

# 4D Printed Programmable Shape-Morphing Hydrogels as Intraoperative Self-Folding Nerve Conduits for Sutureless Neurorrhaphy

Akshat Joshi, Saswat Choudhury, Vageesh Singh Baghel, Souvik Ghosh, Sumeet Gupta, Debrupa Lahiri, G. K. Ananthasuresh, and Kaushik Chatterjee\*

There are only a few reports of implantable 4D printed biomaterials, most of which exhibit slow deformations rendering them unsuitable for in situ surgical deployment. In this study, a hydrogel system is engineered with defined swelling behaviors, which demonstrated excellent printability in extrusion-based 3D printing and programmed shape deformations post-printing. Shape deformations of the spatially patterned hydrogels with defined infill angles are computationally predicted for a variety of 3D printed structures, which are subsequently validated experimentally. The gels are coated with gelatin-rich nanofibers to augment cell growth. 3D-printed hydrogel sheets with pre-programmed infill patterns rapidly self-rolled into tubes in vivo to serve as nerve-guiding conduits for repairing sciatic nerve defects in a rat model. These 4D-printed hydrogels minimized the complexity of surgeries by tightly clamping the resected ends of the nerves to assist in the healing of peripheral nerve damage, as revealed by histological evaluation and functional assessments for up to 45 days. This work demonstrates that 3D-printed hydrogels can be designed for programmed shape changes by swelling in vivo to yield 4D-printed tissue constructs for the repair of peripheral nerve damage with the potential to be extended in other areas of regenerative medicine.

including healthcare.<sup>[1,2]</sup> This emerging technology enables the fabrication of complex and dynamic structures, which are otherwise difficult to realize using conventional 3D printing.<sup>[3,4]</sup> 4D printing utilizes either smart materials that respond to specific stimuli,<sup>[5,6]</sup> programmed design during printing,<sup>[7,8]</sup> or a combination of both.<sup>[9–11]</sup> There is a wide range of smart materials that respond to stimuli,<sup>[12,13]</sup> such as changes in pH,<sup>[14,15]</sup> temperature,<sup>[16]</sup> light,<sup>[17,18]</sup> moisture,<sup>[19,20]</sup> magnetic field,<sup>[21,22]</sup> and so on. In recent years, the rapid advancements in tissue engineering combined with an expanded choice of biomaterials have motivated research in 4D printing for regenerative medicine.<sup>[23–25]</sup> However, the fabrication of complex constructs that faithfully mimic tissue architecture persists as a challenge. Hydrogels are the ideal candidates for engineering tissue scaffolds,<sup>[26,27]</sup> owing to their biocompatibility, high water-absorption capacity, and chemical tunability. Nevertheless, the choice of hydrogels for 4D printing is rather limited owing to their poor

## 1. Introduction

4D printing is trending in the rapidly growing field of additive manufacturing with the prospect of impact in several domains,

printability and shape fidelity and the limited choice of stimuli that are physiologically relevant while exhibiting good biocompatibility.<sup>[28,29]</sup> Moreover, controlling the time scale and

A. Joshi, S. Choudhury, K. Chatterjee  
Centre for Biosystems Science and Engineering  
Indian Institute of Science  
Bangalore 560012, India  
E-mail: kchatterjee@iisc.ac.in

V. S. Baghel, G. K. Ananthasuresh  
Department of Mechanical Engineering  
Indian Institute of Science  
Bangalore 560012, India

S. Ghosh, D. Lahiri  
Biomaterials and Multiscale Mechanics Lab  
Department of Metallurgical and Materials Engineering  
Indian Institute of Technology Roorkee  
Roorkee 247667, India

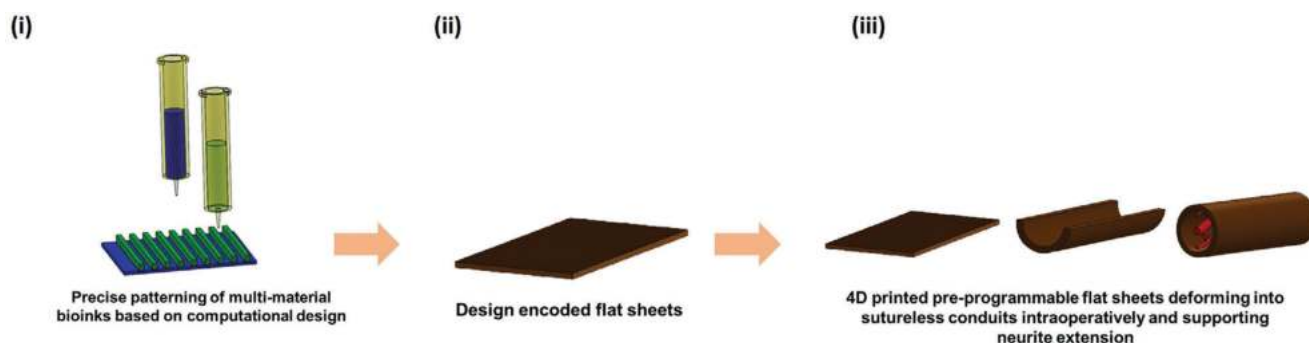
S. Ghosh  
Molecular Endocrinology Lab  
Department of Biotechnology  
Indian Institute of Technology Roorkee  
Roorkee 247667, India

S. Gupta  
Department of Pharmacy  
Maharshi Markandeshwar University  
Mullana 133207, India

K. Chatterjee  
Department of Materials Engineering  
Indian Institute of Science  
Bangalore 560012, India

 The ORCID identification number(s) for the author(s) of this article can be found under <https://doi.org/10.1002/adhm.202300701>

DOI: 10.1002/adhm.202300701



**Scheme 1.** Process of fabrication of 4D printed nerve conduits with intraoperative shape deformation capability. i) 3D printing of multi-material bioinks with precise patterning based on computational design. ii) 3D printed design encoded flat hydrogel sheets. iii) Intraoperative deformation of hydrogel sheet into nerve conduits demonstrating capability for neurite extension and nerve regeneration.

tendency of deformation is often challenging, as it necessitates smart design.<sup>[30]</sup>

A critical limitation of 3D printing is the static nature of the fabricated hydrogels, requiring surgical implantation.<sup>[31]</sup> This strategy demands inconvenient surgical sutures that are often accompanied by complications, including additional traumatic damage and severe inflammation around the injured tissue.<sup>[32]</sup> 4D printing offers a promising route to generate dynamic shape-morphing geometries out of static parts while leveraging the benefits of near-net-shape manufacturing of complex and patient-specific parts. Target designs are encoded during the printing process, which governs the resulting shape deformations post-printing. Hydrogels can swell in response to water uptake and hence, are the material of choice by researchers developing 4D printed biomaterials. Few recent studies report shape deformations of hydrogels, primarily governed by anisotropic swelling, gradients in cross-linking densities, etc. However, their applications *in vivo* are limited due to poor control on programming specific shape deformations in constructs prepared from a single material,<sup>[28,33]</sup> the prolonged time required for the deformations,<sup>[29]</sup> complex bioink preparation,<sup>[34]</sup> and poor control on processes to impart anisotropy within the materials.<sup>[35–37]</sup> These drawbacks hinder the widespread adoption of 4D printed gels for applications necessitating intraoperative shape deformations of deployable devices in minimally-invasive procedures. *In vivo* 3D printing of scaffolds for tissue regeneration has been demonstrated,<sup>[38]</sup> but 4D printed hydrogels with *in vivo* shape-morphing ability are yet to be realized. Among several potential biomedical applications, self-folding nerve conduits that alleviate tedious suturing could benefit the large patient population requiring microsurgery for nerve repair.<sup>[39]</sup>

Shape change of 3D printed hydrogels is primarily governed by the material characteristics that induce differential swelling<sup>[23,34]</sup> and through the programmed design of the printed parts for predetermined controlled deformations.<sup>[7,8]</sup> Analytical models to predict and elucidate the changes are challenging to formulate, owing to the large and geometrically nonlinear deformations. Computational models have been proposed to semi-quantitatively elucidate the deformations for a designed part.<sup>[7]</sup>

In this work, we present a dual-component hydrogel system prepared from alginate and methyl cellulose (A/MC), wherein the fractions of the two components were tuned to obtain gels of different swelling ratios. A model was developed to predict shape de-

formations for parts prepared using these hydrogel formulations. Validation of the model was attempted by correlating the deformations of a wide variety of gel constructs fabricated by extrusion-based 3D printing. The cytocompatibility was assessed, and surface modification by deposition of nanofibers was explored to augment the cellular response to the 4D printed gel. Toward clinical translation of the 4D-printed gel as sutureless nerve guiding conduits (NGCs), the printed gel sheets were implanted to form conduits by *in situ* shape change in a rat sciatic nerve defect model (**Scheme 1**). Nerve regeneration mediated by the sutureless conduits was assessed up to  $\approx 6$  weeks post-implantation. Overall, the study aimed to establish the promise of 4D printed *in vivo* self-rolling conduits for peripheral nerve regeneration.

## 2. Results and Discussion

A dual-component hydrogel system was utilized in this work. Two formulations of A/MC were prepared with different fractions of A and MC such that one resulting gel (A/MC: 3/9 by mass prepared in deionized [DI] water) exhibited a higher swelling rate, and the other (A/MC: 4/6 in 5 mM  $\text{CaCl}_2$  solution) exhibited a relatively lower swelling rate. These compositions were identified after careful evaluation of the printability and swelling rates of several formulations. The physicochemical properties of the individual gels were characterized initially. Morphological analysis by scanning electron microscopy (**Figure 1a**) revealed that the gels were highly porous with interconnected pores. Notably, A/MC:3/9 contained bigger pores than A/MC:4/6, as evident from the cross-sectional SEM micrographs in Figure S2, Supporting Information. This trend corroborates the swelling measurements (**Figure 1b**), which show that A/MC:3/9 swells considerably more than A/MC:4/6.

Rheological characterization to assess the printability and viscoelastic behavior of the gels confirmed the shear-thinning behavior of both hydrogels (**Figure 1c**), rendering them suitable for extrusion-based 3D printing.<sup>[40,41]</sup> **Figure 1d** reveals the viscoelastic properties of the gels with storage moduli values higher than loss moduli in the entire linear viscoelastic (LVR) region. **Figure 1e** shows that the gels were thixotropic such that the viscosities of both the gels decrease under high shear rates and consequently recover to the original values upon releasing the stress. This property endows the gels with good printing fidelity and is

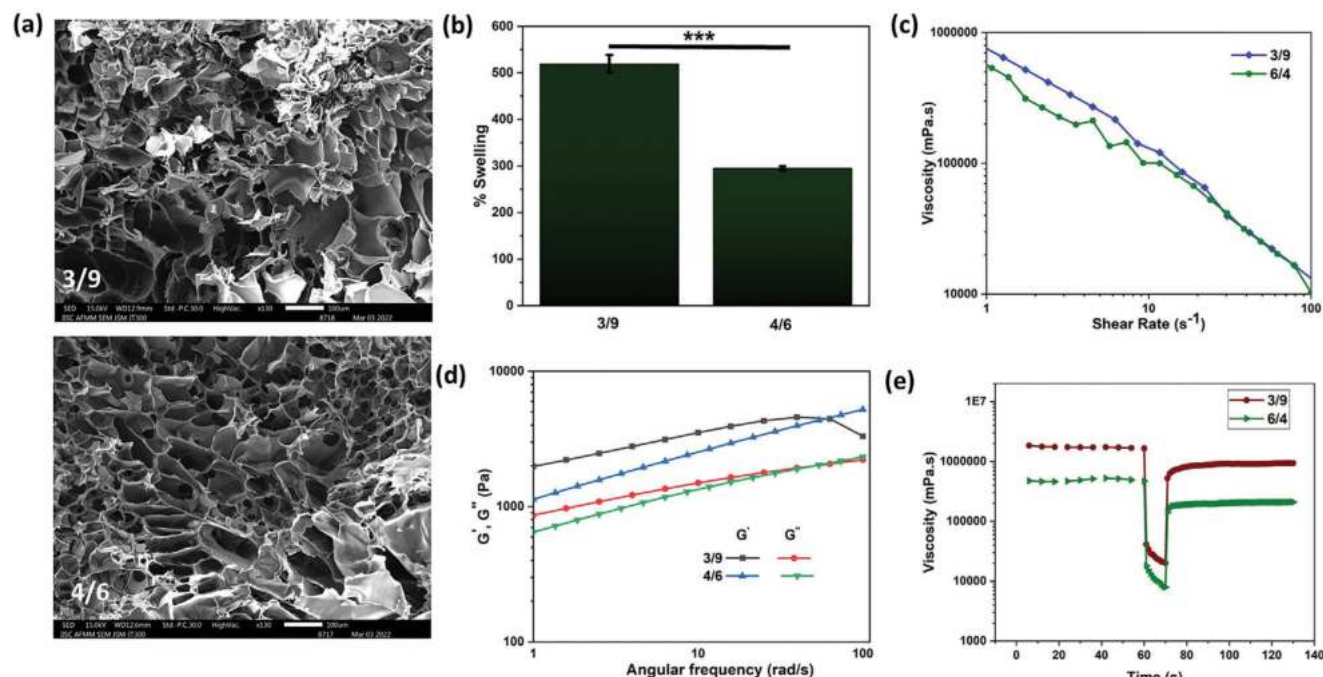


**Figure 1.** Characterization of the A/MC: 3/9 and 4/6 hydrogels. a) SEM image revealing that both gels are porous (Scale bars are 100 μm); b) Swelling ratios for the two gels; c–e) Rheological analysis of the gels; c) Shear-thinning behavior, d) viscoelastic properties of the two gels, and e) thixotropic properties of the two gels. (\*\*\*) denotes  $p < 0.001$ .

a consequence of chain disentanglements and re-entanglements simultaneously under high and low shear rates, respectively.<sup>[42,43]</sup>

A computational model was formulated to reliably predict the different shape deformations of the 3D printed structures with defined infill patterns. We used a thermal expansion model to simulate the deformations of the hydrogels after establishing a quantitative correlation between the swelling model. The details of the model used are provided in the Supporting Information (Section S1, Supporting Information). We proceeded with modeling the deformations of flat structures with different topographies.

At first, the effect of the topography of the top layer on the shape deformation was evaluated by designing a simple tri-layered trapezoidal geometry. The first layer was a solid base material of higher expansion coefficient, which was decorated with stripes of the second material of lower expansion coefficient placed precisely at different orientations with respect to the base layer (Figure 2a[i–iii]). The expansion coefficients for the two materials were calculated from the swelling ratios of the two gels. FEA (finite element analysis) simulations (Figure 2a[iv–vi]) revealed that a trapezoid could deform remarkably differently for the varied arrangements between the two layers, namely, bending along the longer axis for stripes placed parallel (or at 0°) with respect to the long axis of the base layer, twisting for stripes at 45°, and bending along the shorter axis for stripes at 90°. To validate the results determined from the computational model, we designed G-codes to match the computational design (refer to Figure 2b[i–iii]) with details for each layer compiled in Figure S7, Supporting Information. An extrusion-based 3D printer with two nozzles for the two gel formulations was used to print the gels following these G-codes for three different designs. The printed

structures were air-dried for 8–10 h and subsequently swelled in 200 mM  $CaCl_2$  solution to initiate the shape deformation. The resultant deformations are compiled in Figure 2b(iv–vi), revealing that the deformations indeed occurred differently and closely matched the computed results. The real-time deformations were recorded (refer to Videos S1–S3, Supporting Information).

To further validate the accuracy of the model in predicting the shape deformations of the 3D printed gels, we designed a variety of complex geometries with varied infill patterns (G-codes shown in Figure S8, Supporting Information). A cross (or plus cross) construct was designed such that the stripes of the top layer were placed at different angles with respect to the base layer, as shown in Figure 3a(i,ii). As seen from simulations, the cross geometry can be predetermined to bend or twist by varying the arrangement of the stripes (Figure 3a[iii,iv]). Gels were 3D printed with corresponding G-codes (Figure 3b[v,vi]). When the dried gels were allowed to swell in  $CaCl_2$  solution, observed deformations closely matched the deformations determined computationally (refer to Figure 3b[vii,viii] and Videos S4 and S5, Supporting Information). We demonstrated different predetermined modes of deformation in petals governed by defined infill patterns (refer to Figure 3c[i,ii] computational design, [iii,iv] simulated deformation; Figure 3b[v,vi] corresponding G-codes, [vii,viii] corresponding experimental deformation and Videos S6 and S7, Supporting Information). Finally, we investigated the deformation of gels prepared in the shapes of a butterfly and a rectangle (refer to Figure 3e,f and Videos S8 and S9, Supporting Information for the butterfly geometry and Figure 3g,h and Videos S10 and S11, Supporting Information for the rectangular geometry). Toward enhancing the attachment and growth of cells on the gel surface, the dried gel was coated by airbrushing a thin layer of nanofibers

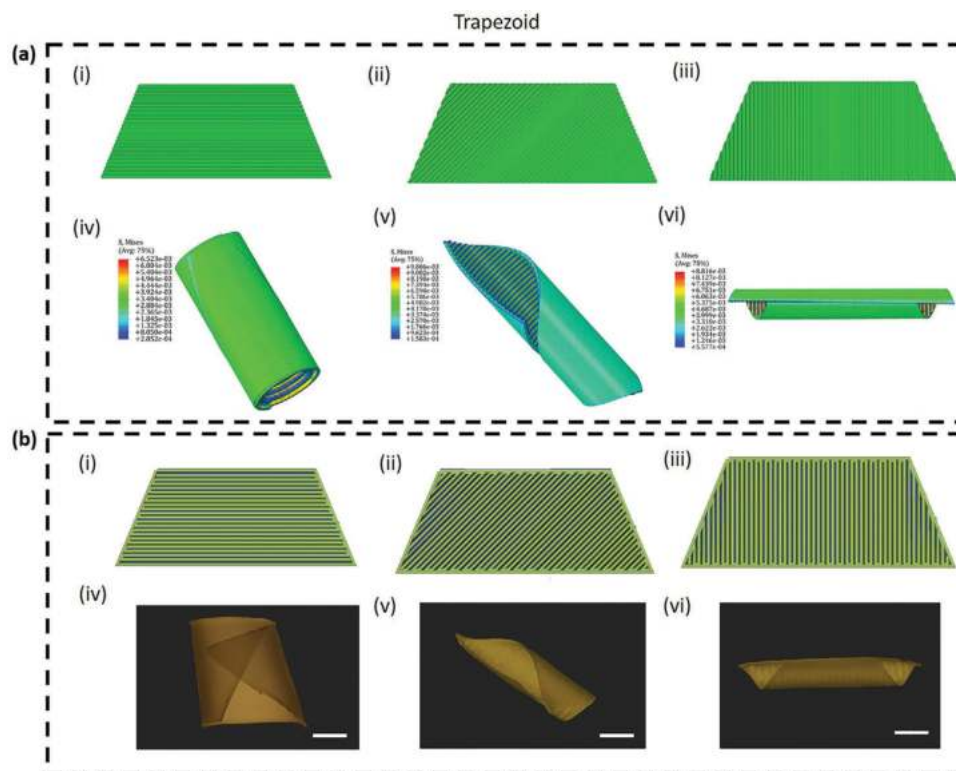


**Figure 2.** FEA simulations and experimental validation of shape deformations. a) Computational analysis wherein (i–iii) are the modeled geometries and (iv–vi) are the corresponding simulated deformations. b) Experimental validation wherein (i–iii) are the modeled G-codes and (iv–vi) represent the digital photographs of the deformed gels. Scale bars: 12 mm.

prepared by blending gelatin and polycaprolactone (PCL). It is to be noted here that the time and tendency of shape deformations were not impacted by nanofiber deposition, as demonstrated in Supporting Information (Section S2, Supporting Information).

We confirmed that our hydrogels (both uncoated and nanofiber-coated gels, hereafter termed uncoated and coated, respectively) were biocompatible *in vitro* and *in vivo* (Section S2, Supporting Information) and that nanofibers do not impact shape deformation (Section S2, Supporting Information). Next, we aimed to demonstrate the clinical benefit of the shape-changing 4D printed hydrogel focusing on its utility as sutureless NGCs. Toward this goal, rectangular models were designed for fabrication by 3D printing to self-roll into tubular constructs of predetermined dimensions upon stimulation with  $\text{CaCl}_2$  solution. Digital photographs of the tubular construct post-deformation and its SEM image are compiled in Figure S9, Supporting Information. Mechanical testing of the 4D-printed nerve conduit was performed to assess the stability and durability under cyclic loading. The stress response of the conduits was marked by hysteresis for the first cycle (Figure S9, Supporting Information) but not in the subsequent nine cycles of loading and unloading, indicating good recovery of the stresses upon unloading with minimal energy losses. Thus, the self-rolled gel matches the biomechanics of soft tissues and is well-suited for engineering NGCs.

Several artificial conduits for nerve regeneration have been developed, some of which have been approved for clinical use by the Food and Drug Administration (FDA).<sup>[44]</sup> In both preclin-

ical and clinical trials, the single tubular structure, NeuraGen and Neurolac, derived from type I collagen and PCL, respectively, showed promising outcomes.<sup>[45]</sup> However, both of these commercially-available conduits require suturing. Even though sutures are widely accepted as the standard therapy for peripheral nerve injury (PNI), they are not without risk, including further traumatic injury and severe inflammation surrounding the wounded nerve tissues, preventing effective regeneration of the nerve.<sup>[46]</sup> Hence, in an attempt to establish a rapid and efficient neurorrhaphy treatment for improving prognosis without any severe inflammatory complications, the 4D printed conduit designed in this study was assessed for potential sutureless neurorrhaphy in PNI treatment.

Owing to its biocompatibility, biomechanical properties, and rapid self-rolling ability upon stimulation, we posited that the 4D-printed rectangular gel sheets could be placed at the injury site to self-roll into a conduit *in vivo* for covering the severed ends of the resected nerve. Such an intraoperative 4D-printed device could offer a marked advantage over the current technology by reducing the complexity and duration of surgeries to facilitate axonal growth and eventual regeneration and restoration of nerve function. The efficacy of 3D-printed gel sheets (with and without the nanofiber coating) as intraoperative deployable implanted nerve conduits was assessed in a well-established 2 mm sciatic nerve defect model in Sprague–Dawley rats and evaluated for up to 6 weeks (Figure 4a). The animals were randomly segregated into four different groups, namely, sham, negative, and uncoated and coated 4D printed gels. No surgical damage was done to the



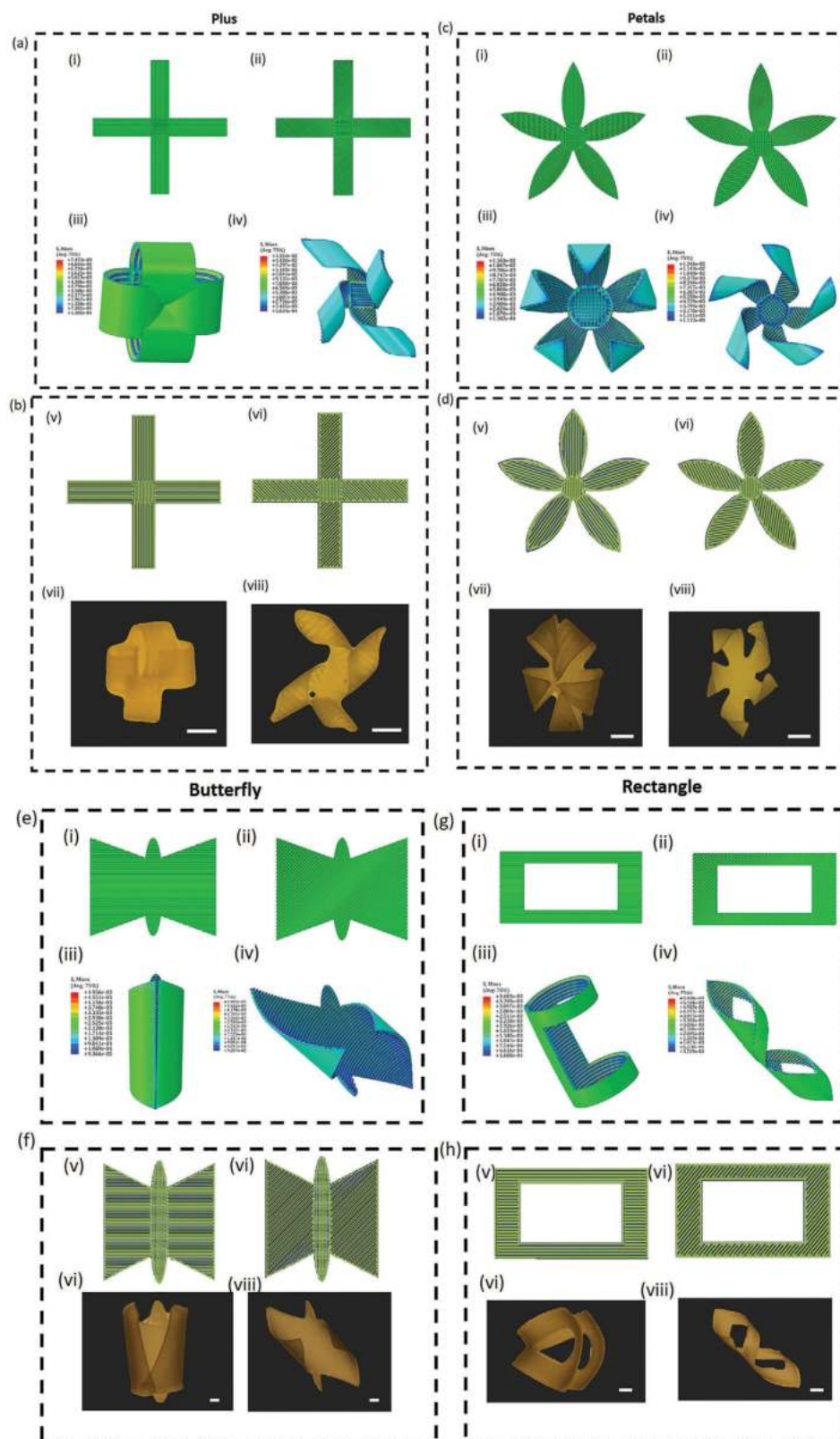


**Figure 3.** FEA simulations and corresponding experimental validation for different geometries. a) Computational evaluation for a cross-shaped geometry; i,ii) Design showing different stripe angles, and iii,iv) Effect of stripe angle on corresponding deformations determined computationally. b) Experimental validation; v,vi) The G-codes created based on computational designs, and vii,viii) The resultant deformations validated experimentally. c) Computational evaluation for a petal-shaped geometry; i,ii) Design showing different stripe angles and iii,iv) effect of stripe angle on the corresponding. d) Experimental validation; v,vi) The G-codes created based on computational designs, and vii,viii) The resultant deformations validated experimentally. e) Computational evaluation for a butterfly-shaped geometry; i,ii) Design showing different stripe angles and iii,iv) effect of stripe angle on the corresponding. f) Experimental validation; v,vi) The G-codes created based on computational designs, and vii,viii) The resultant deformations validated experimentally. g) Computational evaluation for a rectangle-shaped geometry; i,ii) Design showing different stripe angles and iii,iv) effect of stripe angle on the corresponding. h) Experimental validation; v,vi) The G-codes created based on computational designs, and vii,viii) The resultant deformations validated experimentally.

animals in the sham group. Self-healing damage served as the negative control. The procedure of wound infliction and the in vivo shape deformation are presented in Figure S10, Supporting Information. The hydrogel-wrapped regions of the transected sciatic nerves 6 weeks post-surgery are shown in Figure 4b. No animals were lost during the test period. A combination of functional and structural assessments was analyzed to determine the success of nerve regeneration. Functional assessments such as the sciatic function index (SFI), hot plate latency, and paw withdrawal threshold were performed at specific intervals for 6 weeks, following which rats were sacrificed to assess the restoration of motor function in the wound-inflicted leg.

SFI measures the level of activity in the sciatic nerve. SFI was calculated by comparing the geometric representation of the damaged hind paw of an injured rat and the representation of the contralateral paw. Herein, the paw prints of the operated legs and their corresponding contralateral paws of the animals from all the groups were taken on the 1<sup>st</sup>, 15<sup>th</sup>, 30<sup>th</sup>, and 45<sup>th</sup> days (compiled in Figure 4c). In contrast to the negative control group, both the conduit-treated groups showed significant increments in SFI measurements 15<sup>th</sup> day onward post-surgery (Figure 4d). The best SFI values for both the conduit groups were observed on day 45. But among the two groups, the coated group showed a significantly increased SFI, demonstrating the superiority of coated nanofibers. (Figure 4d).

Atrophy of the gastrocnemius muscle (GA) is a common side effect of sciatic nerve damage.<sup>[47]</sup> Muscle atrophy is reduced by the regeneration of the sciatic nerve and reinnervation of the GA. GA weight analysis was used to evaluate muscle atrophy and regeneration. After the animals were sacrificed, the gastrocnemius muscles of both hind legs were removed and weighed. The left (L) (muscle weight of operated left leg)/ right (R) (muscle weight of normal right leg) ratio was determined for all the groups (Figure 4e). After weighing, the lowest L/R ratio was observed for the negative group, whereas it was markedly improved in the case of conduit-treated groups. No significant difference in the L/R ratio was observed among the two conduit groups (Figure 4e). This observation was corroborated by the digital photographs of the gastrocnemius muscles (Figure S11, Supporting Information). Muscle atrophy and regeneration assessed by hematoxylin and eosin (H&E) staining of the GA muscle (Figure 4f) indicated that the mass, integrity, and morphology of the muscle were considerably lost in the negative group (Figures 4f-ii,g). These parameters were markedly improved in animals treated with the 4D printed conduits following the sciatic nerve injury (Figures 4f [iii,iv], g), which were comparable to the sham group. Thus, both conduits (coated and uncoated) repaired the sciatic nerve, reinnervating the gastrocnemius muscle and reducing muscular atrophy as a result of regeneration.

The hot plate and Randall–Selitto tests were used to assess the efficacy of conduits in restoring functional motor activity. In the hot plate study, the amount of time that each animal was

able to withstand the heat or wait before displaying a reaction was recorded. When the sciatic nerves of the animals are compromised, the animals have longer latency durations. This period proportionally decreases as the sciatic nerve regenerates. Figure 4h reveals that the maximum latency period was observed in the negative groups during the post-operative six weeks. The heat latency period was significantly reduced in the 4D printed conduit-treated groups, with maximum improvements observed on day 45. On the 45<sup>th</sup> day, the heat latency period for the uncoated and coated conduits was  $\approx 13$  and  $\approx 11$  s, respectively, which were significantly lower than the negative group ( $\approx 24$  s) (Figure 4h). Moreover, animals in the coated conduit group showed a statistically significant reduction in the heat latency period compared to animals in the uncoated group (Figure 4h). The Randall–Selitto (Paw withdrawal threshold) test determines allodynia or neuropathic pain in the animals. Allodynia, a hypersensitivity to a pain signal, is induced by nerve damage as a result of trauma or illness.<sup>[48]</sup> Weights provide quantifiable pressure on the injured leg in the experimental and sham-operated groups. The paw withdrawal threshold is a measure of the pressure at which an animal withdraws its paw (PWT). Figure 4i reveals that pain hypersensitivity was more successfully suppressed when the damaged sciatic nerves were treated with coated or uncoated conduits. The PWT for uncoated and coated conduits were  $\approx 15$  and  $\approx 16$  g, respectively, on day 45 post-injury. The PWT for the negative group was  $\approx 6$  g. The 135% and 150% improvement observed in the uncoated and coated conduits, respectively, compared to the negative group, demonstrates the functional recovery of the resected sciatic nerve with the 4D printed nerve conduit deployed intraoperatively. However, no significant difference in PWT was observed between the uncoated and coated groups.

The low levels of the biochemical marker, immunoglobulin IgE, eliminated adverse immunogenic responses induced by the implanted conduit (Table S3, Supporting Information). Histological analysis of organs, including the liver and the kidney, further confirmed the cytocompatibility of the implanted hydrogel (Figure S12, Supporting Information).

Histological investigation of the different groups revealed the success of nerve tissue regeneration. Regenerated nerve tissue was observed in the longitudinal slices of samples stained with H&E six weeks post-surgery (Figure 5a,b). Here, the staining of the negative control group is excluded, as no nerve connection was established between the two resected ends. H&E staining of the cross sections (Figure 5a[i-vi]) and longitudinal sections (Figure 5A[vii-ix]) in the middle of the region covered by the conduit shows that nerves and Schwann cells (SCs) were developing into the transplanted conduit, demonstrating that the injured nerves were being regenerated at the proximal end. Quantification of the H&E-stained positive area of the nerve from uncoated (Figures 5a[ii,v,viii],b) and coated conduit groups (Figure 5a[iii,vi,ix],b) confirmed more regenerating nerve fibers in the coated conduit group than in the uncoated group.

deformations determined computationally. d) Experimental validation; v,vi) The G-codes created based on computational designs, and vii,viii) The resultant deformations validated experimentally. e) Computational evaluation for a butterfly-shaped geometry. i–iv) Stripes placed at different angles can control the wing movement. f) (i–viii) Corresponding G-codes and deformed outcomes of the butterfly wing movement. g) Rectangle-shaped geometry can be designed to deform into complex geometries by varying the arrangement of stripes; i–iv) Computational design and deformations. h) Deformed gel of rectangular shape geometry; v–viii) G-codes and corresponding to deformations observed experimentally. Scale bars: 5 mm.

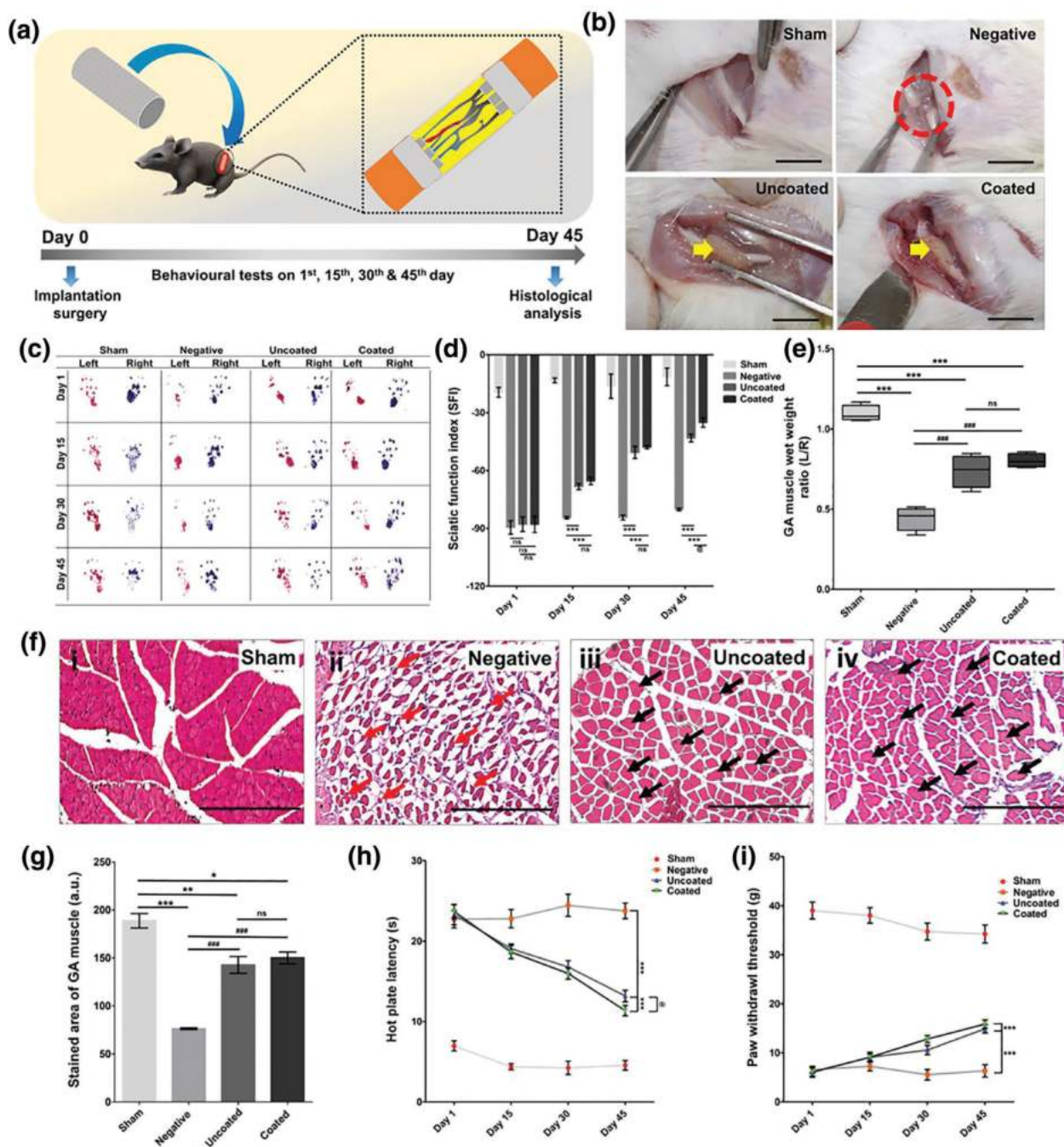


**Figure 4.** Direct and indirect functional assays to assess the regeneration capability of the scaffolds. a) Schematic diagram of implanting scaffolds into sciatic nerve transected SD rat model. b) Digital images of scaffold implantation site taken on 45<sup>th</sup> day after the surgery in different groups (Scale bar: 1 cm). Yellow arrow indicates the area of wrapped scaffolds. Red dotted circle indicates the non-regenerated damaged nerve in the negative group. c) Digital images of the footprints of the left and right hind foot. Individual photos of left and right paw prints of animals from different groups at each time point were assembled to create the image. Red-colored paw print: Left hind leg; Blue-coloured paw print: Right hind leg. d) Quantitative estimation of SFI of different groups at each time point. (\*\*\* denotes  $p < 0.001$  vs negative; @ denotes  $p < 0.05$  vs uncoated). e) Measurements of the gastrocnemius muscle (GA) wet weight ratio (left/right). (\*\*\* denotes  $p < 0.001$  vs sham; ### denotes  $p < 0.001$  vs negative). f) (i–iv) H&E-stained images of the GA muscle of the left hind leg (operated limb) of rats from different experimental and sham groups. (Scale bar: 200  $\mu$ m). The degenerated muscle fibrils (in the negative group) and the regenerated muscle fibrils (Uncoated and coated groups) have now been indicated with red and black arrows respectively. g) Quantification of H&E-stained area of the GA muscle. Data are presented as mean  $\pm$  SD. (n = 4). (\*, \*\*, and \*\*\* represent  $p < 0.05$ ,  $p < 0.01$ , and  $p < 0.001$ , respectively vs sham; ### denotes  $p < 0.001$  vs negative). h) Graph representing the hot plate latency periods of the animal from different groups. Data are presented as mean  $\pm$  SD. (n = 4). (\*\*\* denotes  $p < 0.001$  vs negative; @ denotes  $p < 0.05$  vs uncoated). i) Graph representing the paw withdrawal threshold (PWT) of the animal from different groups. Data are presented as mean  $\pm$  SD. (n = 4). (\*\*\* denotes  $p < 0.001$  vs negative). (ns: non-significant).



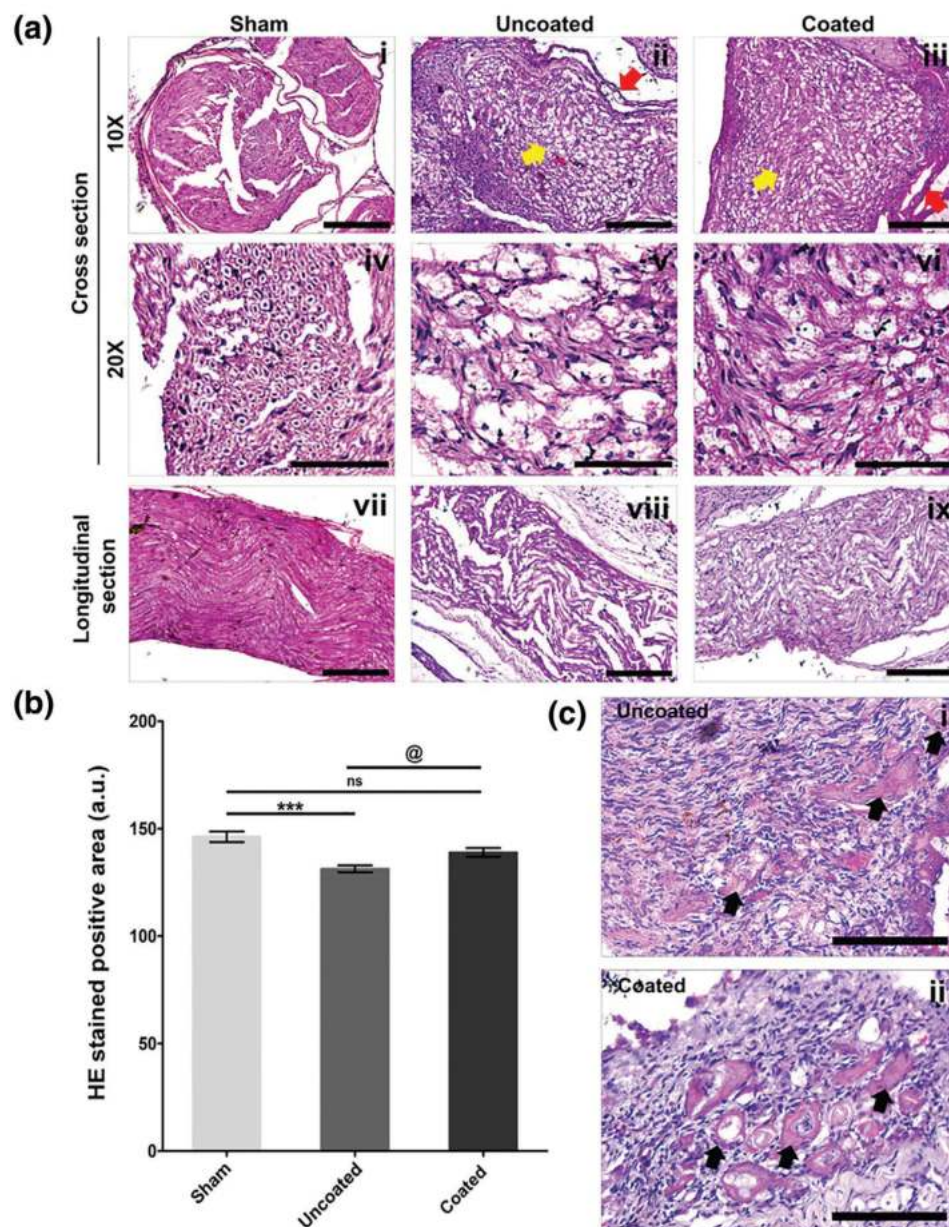


**Figure 5.** Assessment of the nerve regeneration potential of conduits (coated and uncoated) through histological analysis. a) Bright-field pictures of H&E-stained transverse slices of sciatic nerves of rats belonging to various groups: i,iv,vii) sham, ii,v,viii) uncoated, and iii,vi,ix) coated group. Scale bar for (i–iii) and (vii–ix): 200  $\mu$ m; Scale bar for (iv–vi): 50  $\mu$ m. Yellow arrows indicate the regenerated nerve area; red arrows indicate the remnant scaffolds. b) Quantification of H&E stained positive area. Data are presented as mean  $\pm$  SD. ( $n = 4$ ). (\*\*\*) denotes  $p < 0.001$  vs sham; @ denotes  $p < 0.05$  vs uncoated). c) H&E-stained sections of the remnant of the wrapped scaffolds in the nerve injury area. Black arrows indicated the blood vessels. Scale bar: 50  $\mu$ m.

The integrity of the regenerated nerve was also better in the coated group (Figure 5a[iii,vi,ix]) compared to the uncoated (Figure 5a[ii,v,viii]) groups. This enhancement in the coated group was possibly due to the biocompatible fibrous coating in the lumen of the formed tube, which mimics the natural extracellular matrix of the tissue. This fibrous coating provided the ideal environment for the Schwann cells to grow on the fibers to utilize them as tracks on which the axon could be regenerated. The findings of the H&E staining demonstrated that the

sham-operated group had intact nerve fibers (Figure 5a[i,iv,vii]). These results confirm that the surface topography of tissue scaffolds played a critical and essential role in guiding the reconstruction of nerves. Furthermore, Figure 5c(i,ii) indicates that blood vessels were formed in both conduits. Blood vessels provide material exchange and enable nourishment to regenerated nerve tissues and SCs, which are essential components for nerve regeneration.<sup>[49–52]</sup> Therefore, both coated and uncoated gels can aid in the healing of damaged peripheral nerves, as they promote



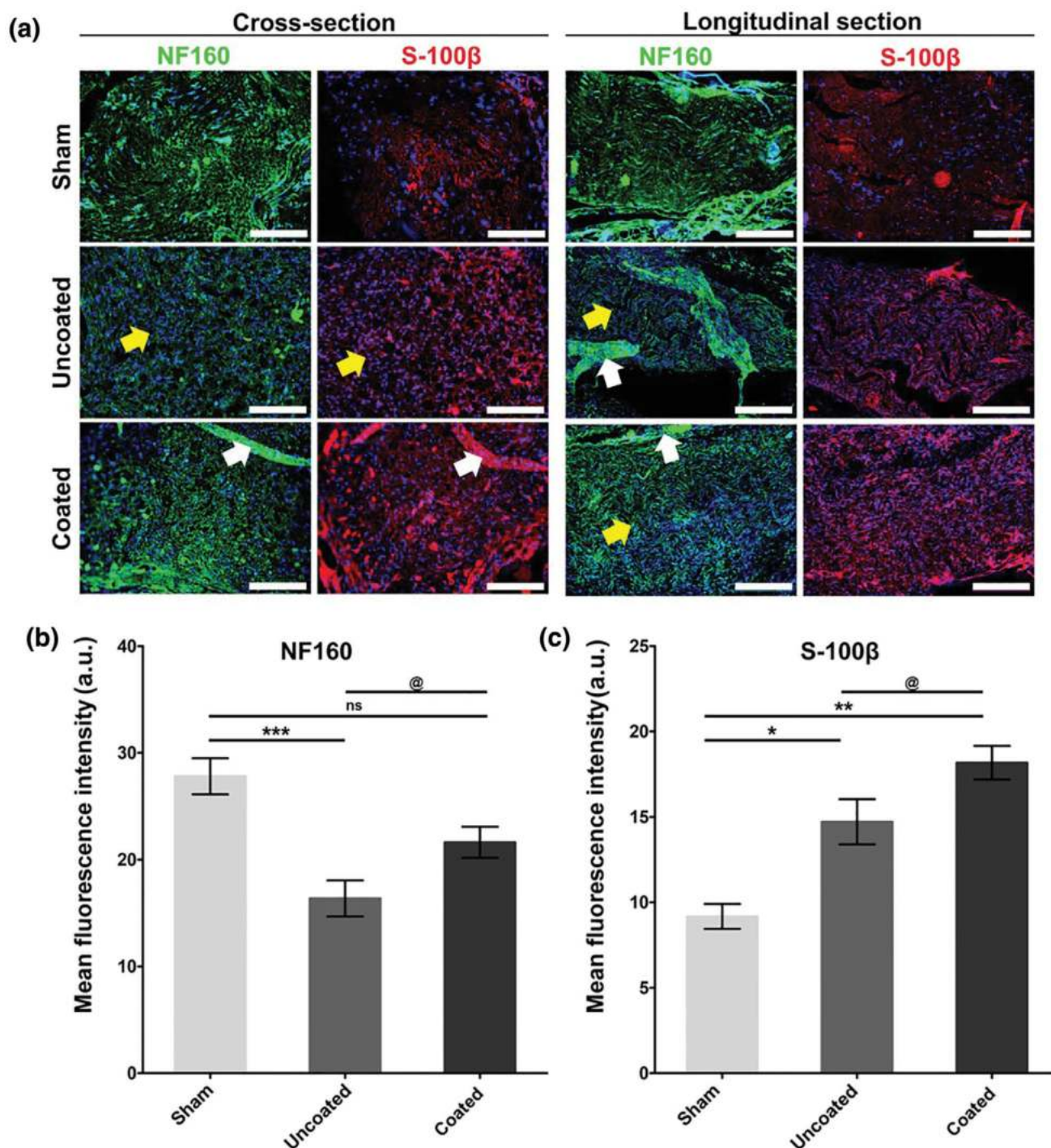


**Figure 6.** Assessment of the nerve regeneration potential of 4D printed conduits through histology. a) Cross-section and longitudinal sections of sciatic nerves were stained for NF-160 (green) (a marker for neurofilaments), S-100 $\beta$  (red) (Schwann cell marker), and nuclei (blue). Scale bar (cross-sections): 100  $\mu$ m; Scale bar (longitudinal sections): 200  $\mu$ m. Yellow arrows indicate the regenerated nerve area; white arrows indicate the remnant scaffolds. Plots of fluorescence intensity for b) NF-160 (\*\*\*) denotes  $p < 0.001$  vs sham; @ denotes  $p < 0.05$  vs uncoated) and c) S-100 $\beta$  (\* and \*\* denotes  $p < 0.05$  and  $p < 0.01$  respectively vs sham; @ denotes  $p < 0.05$  vs uncoated). Data are presented as mean  $\pm$  SD. ( $n = 4$ ).

neovascularization. Nevertheless, further research is warranted to elucidate the underlying mechanisms.

Damage to a peripheral nerve initiates a complex chain of molecular events leading to nerve regeneration. These events include Wallerian degeneration, the axonal response for phagocytosis, chromatolysis, Schwann cell proliferation, axonal growth, and target reinnervation.<sup>[53]</sup> NF160 (Neurofilament 160), a marker for neurofilaments, is typically seen in cells or tissues of neuronal origin. Axonal regeneration requires the presence of SCs. S100 $\beta$  (S100 calcium-binding protein B) is a characteristic marker for SCs. Thus, both the crosssections and the longitudinal sections of the tissues were immunostained for NF-160 (green) and S100 $\beta$  (red), and the nuclei were counterstained with DAPI (**Figure 6a**). NF-160 and S-100 $\beta$  proteins were expressed in all the study groups, confirming the formation of myelin sheaths composed of SCs and the ingrowth of new axons in the 4D printed conduit. The mean fluorescence intensities of both NF-160 and S-100 $\beta$  were calculated by image processing. The highest NF-160 expression was observed in the sham group containing intact nerve fibers. Notably, the expression of NF-160 was higher in the nanofiber-coated conduits than in the uncoated conduits (**Figures 6a [green panels] and 6b**). For S-100 $\beta$ , the sham group showed the least expression as no regeneration occurred, whereas the uncoated and coated conduits showed increased S-100 $\beta$  expression due to tissue regeneration (**Figures 6a [red panels] and 6c**). Notably, the coated group exhibited more expression of S-100 $\beta$  as compared to the uncoated conduit group. Thus, the nanofibrous coating augmented the efficacy of the 4D-printed nerve conduit.

Taken together, the programmable shape-changing hydrogel developed in this work was effective as a 4D-printed NGC. The internal nanofibrous structure further enhanced the conduit performance by altering the gel architecture at both the macroscale and the nanoscale.<sup>[54]</sup> The presence of gelatin in the nanofibers augments cellular interactions, as observed *in vitro*, and could enable the attachment of SCs to the conduit.<sup>[55]</sup> Nanofibers mimic the architectures of extracellular matrices to effectively direct cell fates and functions. Therefore, this fiber-coated gel has the potential to enhance the healing capacity of large-scale lesions in thick nerves.

In a few recent studies, 4D printing has been explored for a few biomaterials, such as silk fibroin methacrylate (SF-MA) and oxidized and methacrylated alginate (OMA). Some of these describe the applicability of the 4D-printed gels *in vivo*. SF-MA was bioprinted into biomimetic trachea-like structures to heal damaged trachea in rabbits.<sup>[23]</sup> However, the utility of these systems is limited by extremely slow shape deformations (the time required was up to 1 h) and poor control of the deformations. Moreover, only one type of bending was observed in a given structure. In stark contrast, we demonstrate the ability to realize several deformations in a single structure by varying infill angles, which can yield a wide range of customized tissue-like structures. Moreover, the shape deformations are much faster in our gels (time scales of a few seconds) which is a vital consideration for intraoperative deployment. Ding et al. 4D printed jammed microflake hydrogels (MFH) into cartilage constructs.<sup>[34]</sup> However, the synthesis of bioinks is complex and is accompanied by prolonged shape deformations ( $\approx 2$  h) and the absence of *in vivo* demonstrations. In particular, cellulose-based bioinks have been recently explored

for 3D/4D printing due to their highly thixotropic properties and ease of synthesis.<sup>[28]</sup> For instance, A/MC gels were shown to exhibit shape changes by varying infill angles,<sup>[8]</sup> however, the system being a single component was not very structurally stable. Moreover, there was no biocompatibility study to support any tissue function, the shape changes were not predicted by any computational model. The multi-component gel system fabricated in this study exhibited differential swelling in addition to design encoded printing paths, which makes the shape changes predictive through modeling, and the resultant structures are robust. Additionally, the gels were surface-modified with nanofibers to make them conducive for cells.

We focused on demonstrating the utility of the 4D-printed multi-component gels for engineering NGCs, which are primarily used to bridge the gap of a severed nerve while guiding the axons to grow and avoiding scar tissue formation.<sup>[56]</sup> So far, most research has focused on 3D-printed gels, such as gelatin methacryloyl (GelMA),<sup>[57]</sup> GelMA/PEGDA,<sup>[58]</sup> and so on., for preparing NGCs. However, 3D-printed NGCs need suturing with the two nerve ends to secure the NGC at the damaged site, which requires highly skilled surgical techniques. The 4D printed NGCs developed here can be placed intraoperatively over the resected nerve ends to self-roll *in vivo*, thereby avoiding the need for suturing. This offers a marked potential clinical advancement over the current techniques. 4D printing can be leveraged to personalize the NGC to customize the diameters and lengths to match patient needs and incorporate complex design features such as branching, which would be otherwise difficult to realize.

### 3. Conclusion

This study presents 4D printable hydrogels that can be programmed to undergo predetermined shape changes *in vivo* after 3D printing for the repair and regeneration of tissues. Dual-component A/MC hydrogels with varied A/MC ratios were 3D printed along different layers with defined infill patterns to spontaneously change their original as-printed shapes when stimulated by water uptake. The shape changes initially computed from FEA simulations were validated experimentally to generate a variety of complex geometries. The gels were coated with gelatin-rich nanofibers for enhanced cell adhesion. 4D printed tubular geometries were obtained by controlled shape deformations *in vivo* of the 3D printed gels to serve as intraoperative self-folding NGCs. The 4D-printed conduits clamped the ends of a resected sciatic nerve in a rat model, eliminating the need for suturing. A combination of histological and functional assays established the capability of the 4D-printed conduits for regenerating peripheral nerves following injury. Overall, this study demonstrates the potential of 4D-printed tissue constructs for the repair and regeneration of peripheral nerves and underscores the promise of 4D printing for other applications in regenerative medicine.

### 4. Experimental Section

**Gel Preparation:** The hydrogels were prepared as reported previously with modifications.<sup>[59]</sup> Briefly, for preparing the Alg/MC:3/9 hydrogels, 3% (w/v) alginate acid sodium (Alg; Sigma Aldrich) was added to 4 ml of deionized (DI) water with constant stirring at 60 °C to obtain a clear solution.

Next, 9% (w/v) MC (Viscosity 4000 cP; Sigma Aldrich) was added slowly with continuous stirring at 60 °C until MC dissolved completely, and a homogeneous solution was obtained. The resulting solution was then filled in a cartridge used for 3D printing and was kept at 4 °C for 30 min for complete hydration of MC, following which the cartridge was stored at room temperature (RT, ≈25 °C) until further use. For preparing the Alg/MC:4/6 gels, a similar procedure was adopted with 5 mM CaCl<sub>2</sub> solution as the medium.

**Gel Characterization:** The pore morphology of both the gels (Alg/MC:3/9 and Alg/MC:4/6) was characterized using a scanning electron microscope (SEM, JEOL iT 300). The gels were lyophilized and sputter-coated with gold before observation. Swelling studies were performed after drying the gels overnight. The initial dry weight ( $W_0$ ) of the gels was measured and then soaked in 200 mM CaCl<sub>2</sub> solution. The weight ( $W_t$ ) of the gels was monitored at regular intervals. The extent of swelling was calculated using the equation.

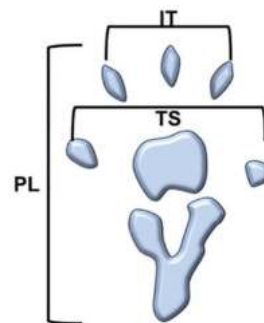
$$\text{Swelling (\%)} = \frac{W_t - W_0}{W_t} \times 100 \quad (1)$$

The viscoelasticity of the gels was characterized using a rotational rheometer (Anton Paar Modular Compact Rheometer- 302) with a 10 mm parallel plate and a 1 mm gap. For the viscosity flow test, the viscosity of the gels was measured at shear rates ranging from 1 to 100 s<sup>-1</sup>. For the angular frequency sweep, a constant strain of 1% was chosen from the linear viscoelastic region (LVR), and angular frequency was varied from 1 to 100 rad s<sup>-1</sup>. Thixotropy characterization was performed in three steps: a low shear rate of 0.1 s<sup>-1</sup> was applied to the gels for 60 s, the shear rate was increased to 100 s<sup>-1</sup> for 10 s, and finally, the shear rate was lowered to 0.1 s<sup>-1</sup> for 60 s.

**Finite Element Analysis (FEA) Theory and Simulations:** Different 3D models were prepared in Solidworks (Dassault Systems), which were then imported into the commercially available FEA software package Abaqus 2017 (Simulia 2017) to predict the deformation of the hydrogel designs experimentally.

**4D Printing of Multi-Component Hydrogels:** To enable the process of 4D printing, the 3D models were designed in Solidworks (Dassault System), which were converted to StereoLithography (.Stl) format for slicing to generate G-codes (Repetier Host, Cellink). For creating the G-codes, the print paths were defined as per computational designs, wherein a first solid layer of Alg/MC:3/9 was overlaid by stripes of Alg/MC:4/6 placed at different angles on the second and third layers with respect to the first layer. For creating stripes, 40% aligned rectilinear infill patterns with defined fill angles were used, as per computational design. The resulting G-codes were then input to an extrusion-based 3D bioprinter (BioX, Cellink) for 3D printing of the gels independently from two nozzles. The printed constructs were air-dried for 8 h at RT and immersed in 200 mM CaCl<sub>2</sub> solution. The resulting shape changes were recorded digitally.

**In Vivo Studies on Sciatic Nerve Transected Model:** All the animal studies were performed in accordance with 86/609/EEC Act with approvals (numbers MMCP-IAEC-120 and MMCP-IAEC-121) from the Institute Animal Ethical Committee of Maharshi Markandeshwar University, Mullana, following globally-accepted norms (NIH Publications no. 8023, revised 1978). Specifically, adult Sprague-Dawley male rats (between 250–270 grams at the time of surgery) were selected to estimate the efficacy of fabricated scaffolds in the regeneration of PNS involving the earlier described sciatic nerve injury model, as described earlier.<sup>[60]</sup> A total of 16 animals were arbitrarily divided into four groups – sham-operated (operational control), negative control (injury without any treatment given), uncoated (4D printed rectangular sheets without any fibers coating), and coated (4D printed rectangular sheets with fibers coating). The resulting dimensions of the self-folding sheets were calculated using simulations to yield conduits to sufficiently cover the defect. Each group contained four animals. Sciatic nerve regeneration was investigated in this work using an injury model with a 2 mm transection. Both the coated and uncoated sheets were sterilized through UV irradiation. Before transplantation, the sheets, including coated and uncoated, were stimulated with 200 mM of CaCl<sub>2</sub> solution and placed at the defect site. Thereafter, 5 mm



**Scheme 2.** Schematic diagram of paw indicating the PL, TS, and IT.

CaCl<sub>2</sub> was poured over the sheets to induce self-folding into tubular structures spontaneously around the injured nerve due to the pre-programmed deformation. Intraperitoneal injections of ketamine (90 mg kg<sup>-1</sup>) and xylazine (10 mg kg<sup>-1</sup>) were used to anesthetize the animals, followed by a bilateral incision at the left lateral thigh. The sciatic nerve was uncovered by cutting through the biceps femoris and gluteus superficial muscles. Each rat had a 2 mm nerve deficit, which was then bridged utilizing different neural scaffolds. Nerve conduits were used to connect the proximal and distal ends of the damaged nerve. As the conduits were wrapped automatically around the wound, thus no suturing was required. A 2-mm segment of the sciatic nerve was removed, and the two ends were left untreated for the negative group. The muscle and skin layers were appropriately sutured with 30 nylon sutures after the implant site had been cleaned and disinfected. To avoid infection, each rat was administered 800 000 units of penicillin immediately following surgery.

**Functional Recovery Tests:** The functional recovery of the animals was assessed at the 1<sup>st</sup>, 15<sup>th</sup>, 30<sup>th</sup>, and 45<sup>th</sup> days post-operatively using the hot plate test and Randall-Selitto test to assess thermal reactivity and mechanical threshold, respectively. For thermal reactivity assessment, each rat was individually placed on a metal hot plate of 30 × 30 cm held at 45 ± 1 °C. The frequency with which the left paw was lifted in order to balance the weight on the right paw, which was not damaged, was carefully observed as a reaction to thermal allodynia. The lifting of paws as a result of regular movement was disregarded.<sup>[60]</sup>

The Randall–Selitto paw pressure test was performed using an analgesy meter. Increasing mechanical pressure was administered to the experimental rat leg on the medial section of the plantar surface of the left hind paws as late as observing a withdrawal response. For each animal, the amount of pressure that caused a withdrawal reaction was recorded.

**Sciatic Functional Index (SFI):** SFI was determined from this formula.

$$\begin{aligned} \text{SFI} = & -38.3 \times \frac{\text{EPL} - \text{NPL}}{\text{NPL}} + 109.5 \times \frac{\text{ETS} - \text{NTS}}{\text{NTS}} + 13.3 \\ & \times \frac{\text{EIT} - \text{NIT}}{\text{NIT}} - 8.8 \end{aligned} \quad (2)$$

where PL indicates the footprint length, TS denotes the total toe spread, IT stands for intermediate toe spread, E is the injured side, and N represents the distance on the contralateral side.<sup>[61]</sup> Scheme 2 represents the schematic diagram of the paw indicating PL, TS, and IT for a better understanding.

**Tissue Collection:** The animals were sacrificed after 6 weeks post-implantation via dislocation of the cervical vertebrae to harvest the tissues. The surgical site was opened up to isolate the scaffold-wrapped area of the resected sciatic nerve in each rat. After separation, the nerve conduits containing the regenerated neural tissues were fixed with 10% neutral-buffered formalin (NBF) at RT for 24 h. The fixed tissues were used for immunohistochemistry (IHC) and H&E staining. Gastrocnemius muscles of the operated left legs were collected for wet weight measurement and HE staining.

**H&E and IHC Staining:** Six weeks post-implantation, the regenerated nerves in the conduits were examined histologically. 5 μm thick



longitudinal and cross sections were cut from the fixed samples using a microtome (Leica) and embedded in paraffin wax. The sections were deparaffinized with xylene and with a gradient of diluted ethanol (100%, 90%, 70%, and 50%). They were further rehydrated, which was followed by gentle rinsing in tap water and stained with freshly prepared HE.<sup>[62]</sup> The sections were dried and mounted on coverslips in DPX (di-styrene, a plasticizer, and xylene) (SRL, India). A microscope with RGB (Red, Green, Blue) filters (Lionheart LX, BioTek, USA) was used to image the stained sections to observe the morphology of regenerated nerve tissues.

Immunofluorescence was performed on cross-sections and longitudinal sections taken from the central portion of the regenerated tissues in the conduit after staining for NF200 and S-100. The procedure described above for IHC staining was used. After rehydration, antigen retrieval was carried out by incubating for 3 min under moist pressure in sodium citrate buffer (pH 6). After rinsing in Tris-buffered saline (pH 7.6), the sections were dried. 1% BSA was used for 2 h as a blocking agent, followed by overnight incubation with mouse monoclonal NF-160 (Sigma-Aldrich, USA) and rabbit polyclonal S100 (Invitrogen, USA) at 4 °C. The sections were washed with Tris-buffered saline containing 0.1% Tween® 20 Detergent (TBST) and incubated with rabbit anti-mouse IgG (H + L) – fluorescein isothiocyanate conjugate (Thermo, USA) secondary antibody for NF-160 and the goat antirabbit IgG (H + L) – tetramethylrhodamine isothiocyanate conjugate (Thermo, USA) secondary antibody for S100 for 2 h followed by washing with TBST. The sections were counterstained with DAPI (HiMedia). Finally, the samples were observed using an epi-fluorescence microscope (Lionheart LX, BioTek, USA). At least three areas were sampled for each section/group.

**Statistical Analysis:** The results are presented as mean ± standard error for each group. GraphPad Prism 5.04 was used for the statistical analysis (GraphPad Software, USA). One-way ANOVA was used for the statistical analysis, which was then followed by Dunnett and Tukey tests for significance. All analyses were carried out at a 95% confidence level and were considered to be significant at statistical probability  $p < 0.05$ . Statistical significances were denoted as (\*/#/@), (\*\*/##/@@) and (\*\*\*/###/@@@) for  $p < 0.05$ ,  $p < 0.01$ , and  $p < 0.001$ , respectively.

## Supporting Information

Supporting Information is available from the Wiley Online Library or from the author.

## Acknowledgements

A.J. and S.C. contributed equally to this work. The authors acknowledge support from the Science and Engineering Research Board (SERB), Government of India (IPA/2020/000025). A.J. is supported by the IoE Postdoctoral Fellowship of the Indian Institute of Science. S.C. is supported by the Prime Minister's Research Fellowship.

## Conflict of Interest

The authors have filed a patent application. No other conflicts to declare.

## Data Availability Statement

The data that support the findings of this study are available from the corresponding author upon reasonable request.

## Keywords

4D printing, hydrogels, nerve-guiding conduits, peripheral nerve injury, tissue engineering

Received: March 4, 2023

Revised: March 24, 2023

Published online:

- [1] F. Momeni, X. Liu, J. Ni, *Mater. Des.* **2017**, 122, 42.
- [2] J. Choi, O.-C. Kwon, W. Jo, H. J. Lee, M.-W. Moon, *3D Print. Addit. Manuf.* **2015**, 2, 159.
- [3] Z. Ding, C. Yuan, X. Peng, T. Wang, H. J. Qi, M. L. Dunn, *Sci. Adv.* **2017**, 3, 1602890.
- [4] A. Subash, B. Kandasubramanian, *Eur. Polym. J.* **2020**, 134, 109771.
- [5] Y. S. Alshehry, M. Nafea, M. S. M. Ali, H. A. Almurib, *Eur. Polym. J.* **2021**, 159, 110708.
- [6] Y. Y. C. Choong, S. Maleksaeedi, H. Eng, S. Yu, J. Wei, P.-C. Su, *Appl. Mater. Today* **2020**, 18, 100515.
- [7] A. Sydney Gladman, E. A. Matsumoto, R. G. Nuzzo, L. Mahadevan, J. A. Lewis, *Nat. Mater.* **2016**, 15, 413.
- [8] J. Lai, X. Ye, J. Liu, C. Wang, J. Li, X. Wang, M. Ma, M. Wang, *Mater. Des.* **2021**, 205, 109699.
- [9] J. Zhang, Z. Yin, L. Ren, Q. Liu, L. Ren, X. Yang, X. Zhou, *Adv. Mater. Technol.* **2022**, 7, 2101568.
- [10] T. Mu, L. Liu, X. Lan, Y. Liu, J. Leng, *Compos. Sci. Technol.* **2018**, 160, 169.
- [11] H. Wei, Q. Zhang, Y. Yao, L. Liu, Y. Liu, J. Leng, *ACS Appl. Mater. Interfaces* **2017**, 9, 876.
- [12] Y. S. Lui, W. T. Sow, L. P. Tan, Y. Wu, Y. Lai, H. Li, *Acta Biomater.* **2019**, 92, 19.
- [13] P. Rastogi, B. Kandasubramanian, *Chem. Eng. J.* **2019**, 366, 264.
- [14] B. Narupai, P. T. Smith, A. Nelson, *Adv. Funct. Mater.* **2021**, 31, 2011012.
- [15] C. A. Spiegel, M. Hippler, A. Münchinger, M. Bastmeyer, C. Barner-Kowollik, M. Wegener, E. Blasco, *Adv. Funct. Mater.* **2020**, 30, 1907615.
- [16] F. Zhang, L. Wang, Z. Zheng, Y. Liu, J. Leng, *Composites, Part A* **2019**, 125, 105571.
- [17] J. del Barrio, C. Sánchez-Somolinos, *Adv. Opt. Mater.* **2019**, 7, 1900598.
- [18] F. M. Yavitt, B. E. Kirkpatrick, M. R. Blatchley, K. S. Anseth, *ACS Biomater. Sci. Eng.* **2022**, 8, 4634.
- [19] K. Zhang, A. Geissler, M. Standhardt, S. Mehlhase, M. Gallei, L. Chen, C. Marie Thiele, *Sci. Rep.* **2015**, 5, 11011.
- [20] H. Chathuranga, I. Marriam, Z. Zhang, J. MacLeod, Y. Liu, H. Yang, C. Yan, *Adv. Mater. Technol.* **2022**, 7, 2100447.
- [21] H. Wu, O. Wang, Y. Tian, M. Wang, B. Su, C. Yan, K. Zhou, Y. Shi, *ACS Appl. Mater. Interfaces* **2020**, 13, 12679.
- [22] X. Wan, Y. He, Y. Liu, J. Leng, *Addit. Manuf.* **2022**, 53, 102689.
- [23] S. H. Kim, Y. B. Seo, Y. K. Yeon, Y. J. Lee, H. S. Park, M. T. Sultan, J. M. Lee, J. S. Lee, O. J. Lee, H. Hong, *Biomaterials* **2020**, 260, 120281.
- [24] C. Cui, D.-O. Kim, M. Y. Pack, B. Han, L. Han, Y. Sun, L.-H. Han, *Biofabrication* **2020**, 12, 045018.
- [25] P. Dorishetty, N. K. Dutta, N. R. Choudhury, *Adv. Colloid Interface Sci.* **2020**, 281, 102163.
- [26] H. Zhao, M. Liu, Y. Zhang, J. Yin, R. Pei, *Nanoscale* **2020**, 12, 14976.
- [27] T. Distler, A. R. Boccaccini, *Acta Biomater.* **2020**, 101, 1.
- [28] M. C. Mulakkal, R. S. Trask, V. P. Ting, A. M. Seddon, *Mater. Des.* **2018**, 160, 108.
- [29] L. Zhang, Y. Xiang, H. Zhang, L. Cheng, X. Mao, N. An, L. Zhang, J. Zhou, L. Deng, Y. Zhang, *Adv. Sci.* **2020**, 7, 1903553.
- [30] A. Zolfagharian, A. Kaynak, S. Y. Khoo, A. Kouzani, *Sens. Actuators, A* **2018**, 274, 231.
- [31] Y. Chen, J. Zhang, X. Liu, S. Wang, J. Tao, Y. Huang, W. Wu, Y. Li, K. Zhou, X. Wei, *Sci. Adv.* **2020**, 6, aba7406.
- [32] H. Cheong, Y.-J. Jun, E. Y. Jeon, J. I. Lee, H. J. Jo, H. Y. Park, E. Kim, J. W. Rhie, K. I. Joo, H. J. Cha, *Chem. Eng. J.* **2022**, 445, 136641.

- [33] A. Kirillova, R. Maxson, G. Stoychev, C. T. Gomillion, L. Ionov, *Adv. Mater.* **2017**, 29, 1703443.
- [34] A. Ding, O. Jeon, D. Cleveland, K. L. Gasvoda, D. Wells, S. J. Lee, E. Alsberg, *Adv. Mater.* **2022**, 34, 2109394.
- [35] I. Apsite, G. Constante, M. Dulle, L. Vogt, A. Caspari, A. R. Boccaccini, A. Synytska, S. Salehi, L. Ionov, *Biofabrication* **2020**, 12, 035027.
- [36] J. Uribe-Gomez, A. Posada-Murcia, A. Shukla, M. Ergin, G. Constante, I. Apsite, D. Martin, M. Schwarzer, A. Caspari, A. Synytska, *ACS Appl. Bio Mater.* **2021**, 4, 1720.
- [37] G. Constante, I. Apsite, H. Alkhamis, M. Dulle, M. Schwarzer, A. Caspari, A. Synytska, S. Salehi, L. Ionov, *ACS Appl. Mater. Interfaces* **2021**, 13, 12767.
- [38] A. Urciuolo, I. Poli, L. Brandolino, P. Raffa, V. Scattolini, C. Laterza, G. G. Giobbe, E. Zambaiti, G. Selmin, M. Magnussen, *Nat. Biomed. Eng.* **2020**, 4, 901.
- [39] J. Wang, H. Xiong, T. Zhu, Y. Liu, H. Pan, C. Fan, X. Zhao, W. W. Lu, *ACS Nano* **2020**, 14, 12579.
- [40] D. Petta, D. W. Grijsma, M. Alini, D. Eglon, M. D'Este, *ACS Biomater. Sci. Eng.* **2018**, 4, 3088.
- [41] M. Shin, J. H. Galarraga, M. Y. Kwon, H. Lee, J. A. Burdick, *Acta Biomater.* **2019**, 95, 165.
- [42] Y. P. Singh, A. Bandyopadhyay, B. B. Mandal, *ACS Appl. Mater. Interfaces* **2019**, 11, 33684.
- [43] A. Bandyopadhyay, B. B. Mandal, N. Bhardwaj, *J. Biomed. Mater. Res., Part A* **2022**, 110, 884.
- [44] A. Singh, S. Asikainen, A. K. Teotia, P. A. Shiekh, E. Huotilainen, I. Qayoom, J. Partanen, J. Seppälä, A. Kumar, *ACS Appl. Mater. Interfaces* **2018**, 10, 43327.
- [45] M. R. MacEwan, E. R. Zellmer, J. J. Wheeler, H. Burton, D. W. Moran, *Front. Neurosci.* **2016**, 10, 557.
- [46] A. Pabari, S. Y. Yang, A. M. Seifalian, A. Mosahebi, *J. Plast., Reconstr. Aesthetic Surg.* **2010**, 63, 1941.
- [47] R. Li, Y. Li, Y. Wu, Y. Zhao, H. Chen, Y. Yuan, K. Xu, H. Zhang, Y. Lu, J. Wang, *Biomaterials* **2018**, 168, 24.
- [48] V. C. Anseloni, M. Ennis, M. S. Lidow, *J. Neurosci. Methods* **2003**, 131, 93.
- [49] A.-L. Cattin, J. J. Burden, L. Van Emmenis, F. E. Mackenzie, J. J. Hoving, N. G. Calavia, Y. Guo, M. McLaughlin, L. H. Rosenberg, V. Quereda, *Cell* **2015**, 162, 1127.
- [50] B. Zhao, Z. Zhao, J. Ma, X. Ma, *Neurosci. Lett.* **2019**, 705, 259.
- [51] R. K. Jain, P. Au, J. Tam, D. G. Duda, D. Fukumura, *Nat. Biotechnol.* **2005**, 23, 821.
- [52] C. Chen, J. Tang, Y. Gu, L. Liu, X. Liu, L. Deng, C. Martins, B. Sarmento, W. Cui, L. Chen, *Adv. Funct. Mater.* **2019**, 29, 1806899.
- [53] A. D. Gaudet, P. G. Popovich, M. S. Ramer, *J. Neuroinflammation* **2011**, 8, 110.
- [54] Y. Zhao, Q. Zhang, L. Zhao, L. Gan, L. Yi, Y. Zhao, J. Xue, L. Luo, Q. Du, R. Geng, *ACS Omega* **2017**, 2, 7471.
- [55] L. Yao, G. C. de Ruiter, H. Wang, A. M. Knight, R. J. Spinner, M. J. Yaszemski, A. J. Windebank, A. Pandit, *Biomaterials* **2010**, 31, 5789.
- [56] A. Faroni, S. A. Mobasser, P. J. Kingham, A. J. Reid, *Adv. Drug Delivery Rev.* **2015**, 82, 160.
- [57] W. Ye, H. Li, K. Yu, C. Xie, P. Wang, Y. Zheng, P. Zhang, J. Xiu, Y. Yang, F. Zhang, *Mater. Des.* **2020**, 192, 108757.
- [58] W. Zhu, K. R. Tringale, S. A. Woller, S. You, S. Johnson, H. Shen, J. Schimelman, M. Whitney, J. Steinauer, W. Xu, *Mater. Today* **2018**, 21, 951.
- [59] D. Podstawczyk, M. Nizioł, P. Szymczyk, P. Wiśniewski, A. Guiseppi-Elie, *Addit. Manuf.* **2020**, 34, 101275.
- [60] T. Dowdall, I. Robinson, T. F. Meert, *Pharmacol., Biochem. Behav.* **2005**, 80, 93.
- [61] J. Bain, S. Mackinnon, D. Hunter, *Plast. Reconstr. Surg.* **1989**, 83, 129.
- [62] S. Ghosh, S. Haldar, S. Gupta, A. Bisht, S. Chauhan, V. Kumar, P. Roy, D. Lahiri, *ACS Appl. Bio Mater.* **2020**, 3, 5796.

# **4D Printed Biocompatible Magnetic Composite for Minimally Invasive Deployable Structures**

Saswat Choudhury<sup>1</sup>, Akshat Joshi<sup>1</sup>, Debayan Dasgupta<sup>2</sup>, Ambarish Ghosh<sup>2,3</sup>, Sonal  
Asthana<sup>4,5</sup>, Kaushik Chatterjee<sup>1,4#</sup>

<sup>1</sup>Centre for BioSystems Science and Engineering, Indian Institute of Science, C.V. Raman  
Avenue, Bangalore, India 560012

<sup>2</sup>Centre for Nanoscience and Engineering, Indian Institute of Science, C.V. Raman Avenue,  
Bangalore, India 560012

<sup>3</sup>Department of Physics, Indian Institute of Science, C.V. Raman Avenue, Bangalore, India  
560012

<sup>4</sup>Department of Materials Engineering, Indian Institute of Science, C.V. Raman Avenue,  
Bangalore, India 560012

<sup>5</sup>Department of Hepatobiliary and Multi-Organ Transplantation Surgery, Aster CMI Hospital,  
Bangalore, India 560024

#Corresponding author:

[kchatterje@iisc.ac.in](mailto:kchatterje@iisc.ac.in); +91-80-22933408



## Abstract

4D printing of shape memory polymers (SMPs) and composites has been realized for a multitude of applications spanning healthcare, soft robotics, environment, space, etc. However, demonstrating such materials for *in vivo* applications has not been possible to a large extent due to the unavailability of suitable materials with recovery temperatures around physiological levels. Also, direct heating to trigger shape recovery in SMPs is not a practical and elegant approach in many cases. In this study, polylactide-co-trimethylene carbonate (PLMC), an SMP, has been endowed with magnetic iron oxide ( $\text{Fe}_3\text{O}_4$ ) nanoparticles to realize remote heating under alternating magnetic field and at temperatures around  $40^\circ\text{C}$ . The PLMC-5%  $\text{Fe}_3\text{O}_4$  composite was 3D printed into a variety of shapes, including scaffolds, fixed into pre-programmed temporary shapes to be deployed minimally invasively, and then recovered into original shapes under magnetic actuation. The shape recovery was excellent ( $>99\%$ ) and fast (under 20-30 s). Additionally, these magnetic composites could potentially be guided to the site of deployment through permanent magnets. Both PLMC and its composites were printed in distinct regions of a single structure, deformed, and then recovered by selective and sequential stimulation of magnetic field and heat, respectively. The materials (both PLMC and its nanocomposite) exhibited favorable *in vitro* and *in vivo* biocompatibility, thus highlighting their usefulness for being used as deployable tissue scaffolds and medical devices, among other implantable applications.

**Keywords:** shape memory polymers; biomaterials; minimally invasive surgery; smart materials; nanocomposites

## 1. Introduction

The field of additive manufacturing has advanced rapidly and is increasingly being adapted to meet the challenging demands of various sectors, including environment<sup>1</sup>, robotics<sup>2</sup>, healthcare<sup>3</sup>, etc. Four-dimensional (4D) printing is the latest addition to this fascinating field. It combines three-dimensional (3D) printing with smart materials. Smart materials used are typically shape-memory polymers (SMPs), which exhibit the unique property of stabilizing a temporary deformed shape and subsequent recovery back to their original shape by the application of an external stimulus<sup>4</sup>. This property stems from the distinct molecular architectures of the polymers. The presence of such distinct phases in the polymer allows it to be fixed into a temporary shape by deformation (governed by netpoints or hard segments) below the transition temperature, followed by recovery into original shape (influenced by molecular switches or soft segments) upon heating it above the transition temperature. Owing to this intrinsic property of temperature-assisted shape recovery, SMPs have been explored for various potential applications, such as soft robotics<sup>5</sup>, grippers<sup>6</sup>, self-deployable structures in space applications<sup>7</sup>, and biomedical applications<sup>8</sup>.

In the field of biomedicine, it is also essential that the SMP being used is biocompatible and preferably biodegradable. There exists only a handful of polymer candidates meeting these stringent requirements, such as polylactic acid<sup>9</sup> (PLA), polyurethanes<sup>10</sup> (PUs), their blends, epoxy-based thermosets<sup>11</sup>, etc. However, these materials are associated with serious drawbacks such as difficult processability, minimal recovery performance, high recovery temperatures, which limits their applicability *in vivo*, etc. SMPs could be useful for facilitating minimally invasive procedures, wherein the fixed and compressed shape can be deployed at the target site, and the SMP can then recover to its original shape upon specific stimulation. SMPs have been proposed for cardiovascular stents<sup>12</sup>, clot removal devices<sup>13</sup>, self-tightening wound closure

devices<sup>14</sup>, etc. When the stimulus used is light, the shape memory function can be combined with laser treatment for photodynamic therapy for cancer<sup>15</sup>.

Poly(lactide-co-trimethylene carbonate) (PLMC), a biodegradable polymer, has been explored as a versatile shape memory polymer in some studies for biomedical applications<sup>16</sup>. The distinct advantage is its glass transition temperature ( $T_g$ ), which lies close to the physiological temperature, rendering it a promising candidate for *in vivo* applications. However, triggering shape recovery through direct heating is not feasible in many cases, particularly for *in vivo* applications requiring intraoperative stimulation. Owing to poor thermal conductivity of the polymers, the entire surrounding region must be heated up, which could take a long time and the shape change may not be uniform. Thus, athermal heating, which is possible by careful selection of the nanofillers incorporated in the polymer matrix, is a potentially viable means of exploiting the shape memory materials for remote actuation. The stimulus could be light<sup>17</sup>, ultrasound<sup>18</sup>, water<sup>19</sup>, microwaves<sup>20</sup>, etc. Magnetic stimulation is a potential means of remote actuation of these materials via indirect heating. The most popular nanofiller in this regard is iron oxide ( $Fe_3O_4$ ) nanoparticles which have an excellent inductive heating ability.  $Fe_3O_4$  nanoparticles have far-reaching applications in biomedicine, including hyperthermia for cancer treatment<sup>21</sup>, magnetic resonance imaging contrast agents<sup>22</sup>, etc. These nanoparticles also have the ability to transfer energy from the radio-frequency field to surrounding media via heat dissipation<sup>23</sup>. However, utilizing  $Fe_3O_4$  nanoparticles to activate recovery of SMPs is barely explored. So far, one study has reported the incorporation of  $Fe_3O_4$  in PLA and crosslinked PLA matrices to yield composites and demonstrated the shape recovery of the composites inside alternate magnetic field<sup>24</sup>. However, the drawback of this material is its high recovery temperatures (70°C), complex chemical modifications to crosslink PLA, difficult processability involving solvents, high filler concentrations, etc. The other few studies based



on PLA and  $\text{Fe}_3\text{O}_4$  composites<sup>25-26</sup> are also not devoid of the mentioned drawbacks which limit their applications *in vivo* as deployable scaffolds.

In this work, PLMC as an SMP has been endowed with  $\text{Fe}_3\text{O}_4$  nanoparticles to realize remote actuation through a magnetic field. PLMC- 5%  $\text{Fe}_3\text{O}_4$  composites were 3D printed via extrusion-based technology into simple two-dimensional (2D) shapes and 3D shapes, including tissue scaffolds (as shown in figure 1). Extrusion printing is advantageous over other modalities like direct ink writing, which requires tedious optimization and longer times for complete removal of solvent from the printed structures<sup>27</sup>, etc. The composites were athermally triggered under an alternating magnetic field, highlighting free as well as restrictive shape memory properties. Dual material printing was also performed to spatially lay down PLMC and its composite in specific parts of the same structure. The dual-printed structures were selectively and sequentially actuated through inductive and direct heating. The materials were tested for thermal properties, shape memory properties, and finally, biological response *in vitro* and *in vivo*.

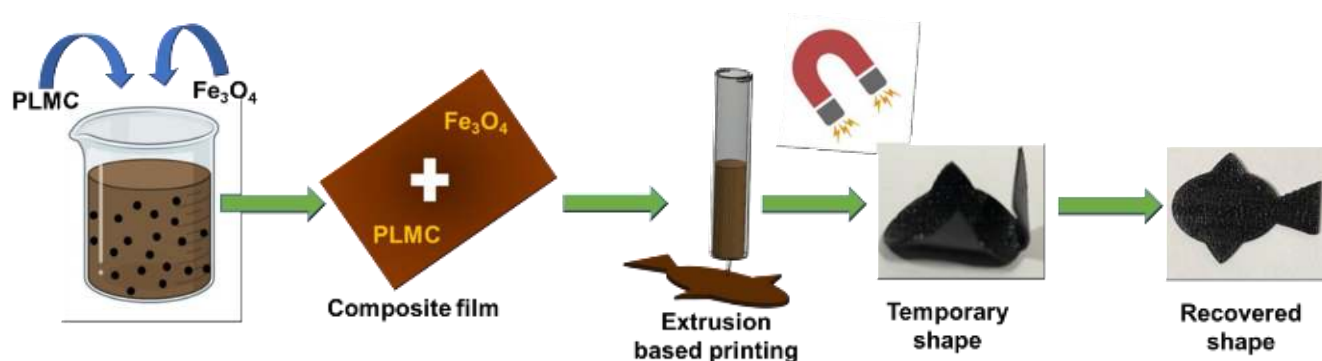


Figure 1: Schematic of the composite preparation and 3D printing followed by magnetic actuation for shape recovery

## 2. Experimental

### 2.1 Materials

PLMC was purchased from Evonik Ltd, Germany. Magnetite nanoparticles (of size range 50-100 nm) were purchased from Sigma Aldrich Pvt Ltd. Dichloromethane (DCM) of analytical grade was purchased from Sigma Aldrich.

### 2.2 Fabrication and 3D printing of PLMC-Fe<sub>3</sub>O<sub>4</sub> nanocomposites

PLMC was dissolved in DCM (0.15 g/mL) under continuous magnetic stirring till a clear homogeneous solution was obtained. Fe<sub>3</sub>O<sub>4</sub> nanoparticles were sonicated in DCM using probe sonication for about 40 min till a well-dispersed suspension was obtained. The suspension was then transferred into the polymer solution, and the resulting solution was further bath sonicated for another 40 min for the particles to homogeneously disperse in the polymer matrix. This solution was then cast over Teflon sheets and left to dry overnight. The composite film, obtained upon drying of the solvent, was then kept inside a vacuum oven for about 48 h to completely remove any traces of solvent present in the film. The obtained film was chopped into smaller pieces and fed inside the metal cartridge of the 3D printer (BioX, CELLINK).

Printing parameters were optimized to get good accuracy and resolution of the composite structures. Printing temperatures were in the range of 200°C to 210°C, the pressure of about 200 MPa, and printing speed ranging between 6 and 7 mm/s.

### 2.3 Thermal characterization

The thermal properties of the polymer and nanocomposite were characterized using a differential scanning calorimeter (DSC, TA Instruments Q 2000). The samples of weight 3-5 mg were scanned between -70°C and 200°C at a scanning rate of 10°C min<sup>-1</sup>. The samples were subjected to a heat-cool-heat cycle to remove any processing history. Thermal

degradation was performed on the samples using a thermogravimetric analyzer (TGA, TA Instruments Q 500). Samples of 3-5mg were heated from 40°C to 800°C at a heating rate of 10 °C min<sup>-1</sup> under an inert atmosphere.

## 2.4 Shape-memory characterization

Shape memory properties of both the 3D printed polymer and composite structures were assessed by performing a shape memory testing cycle using TA instruments-Q800, Dynamic Mechanical Analysis (DMA). The samples for this test were prepared by 3D printing the materials into rectangular strips of 25×6×1 mm<sup>3</sup>. The test was performed in stress-controlled tension mode in the following program:

- i) Deformation: The printed sample was heated to a temperature  $T_d$  (deformation temperature slightly above  $T_g$ ) and equilibrated for 5 min, which gives the initial strain. The sample was then stretched isothermally from 0.001 to 0.025 MPa with a stress ramp rate of 0.005 MPa/min. The strain at this point was denoted as deformed strain ( $\epsilon_{\text{deformed}}$ ).
- ii) Cooling: The sample was then cooled to 0°C (much below  $T_g$ ) at a rate of 5°C min<sup>-1</sup>. It was equilibrated for 5 min under the application of constant force.
- iii) Fixing: The external force was unloaded isothermally at a rate of 0.005 MPa/min. It was again equilibrated at 0°C for 5 min, and the strain captured at this point was fixed strain ( $\epsilon_{\text{fix}}$ ).
- iv) Recovery: The sample was reheated at a rate of 5°C min<sup>-1</sup> to  $T_d$  and equilibrated for 10 min. The recorded strain is indicated as the residual strain after recovery ( $\epsilon_{\text{recov}}$ ). The sample was finally cooled down to 0°C.

$$R_f(\%) = \frac{\epsilon_{\text{fix}}}{\epsilon_{\text{deformed}}} \times 100\%$$

$$R_r(\%) = \frac{\epsilon_{\text{deformed}} - \epsilon_{\text{recov}}}{\epsilon_{\text{deformed}} - \epsilon_{\text{initial}}} \times 100\%$$

## 2.5 Morphological and chemical characterization

Fe<sub>3</sub>O<sub>4</sub> nanoparticles were characterized for their morphology and chemical structure using a scanning electron microscope (Ultra 55 FESEM, Karl Zeiss Mono) and X-ray diffractometer (XRD), respectively. The particles were dispersed homogeneously in ethanol before drop casting over silicon wafers, which were mounted on an aluminum stub, sputter coated with gold, and then imaged under SEM. An accelerating voltage of 4 kV and a secondary electron detector (SE2) was used.

PLAMC- Fe<sub>3</sub>O<sub>4</sub> composites were 3D printed into disc-shaped structures, desiccated, and gold-sputtered before visualization under SEM. PLAMC and PLAMC- Fe<sub>3</sub>O<sub>4</sub> composites were characterized for chemical structure using Fourier transform infrared spectroscopy- attenuated total reflectance (FTIR-ATR) analysis on a Perkin Elmer Fourier spectrometer, USA. The spectra were recorded in the range of 650-400 cm<sup>-1</sup> with a resolution of 4 cm<sup>-1</sup>.

## 2.6 Magnetic field heating of PLMC-Fe<sub>3</sub>O<sub>4</sub> nanocomposites

Magnetic hyperthermia heating was achieved by using the Ambrell Easyheat Induction system (10 kW). The magnetic field generated inside the coil was kept at  $\approx 40 \text{ kA m}^{-1}$  ( $\approx 500 \text{ Gauss}$ ). The magnetic field oscillated at a frequency of 215 kHz. The power delivered at the center of the hyperthermia coil was kept in the range of 3.7 kW to 4.1 kW.

## 2.7 *In vitro* cytocompatibility

NIH-3T3 cells were cultured in DMEM high glucose cell culture media (supplemented with 10% FBS). Sterilized samples were then seeded with fibroblast cells (NIH-3T3) at 8-10 passages at a density of 10,000 cells/cm<sup>2</sup>. Cell growth was monitored using Alamar blue assay following the manufacturer's protocol (Thermo Fisher Scientific, USA). Cells at day 3 post seeding were also stained with Calcein-AM/ Ethidium homodimer (EtDi, EthD-1; Thermo-



fisher scientific, USA) to visually analyze the toxicity of prepared samples. Morphology of seeded cells was also analyzed on Days 3 and 5 using Phalloidin (Alexa fluor 488, Thermo Fisher Scientific, USA)/DAPI (4',6-diamidino-2-phenylindole, Thermo Fisher Scientific, USA) double staining.

## 2.8 *In vivo* biocompatibility assessment

The *in vivo* toxicity of the scaffolds was assessed using Wistar rats. All the animal work was performed in accordance with 86/609/EEC act and approved by the Institute Animal Ethics Committee of the Indian Institute of Science, Bangalore (protocol number CAF/Ethics/878/2022). Adult male Wistar rats aged 8-10 months, weighing 190–230 g, were housed in well-ventilated cages supplied with autoclaved sawdust beddings. Food and sterile water were given ad libitum. 12 h light and dark cycle was maintained in the animal house at  $25 \pm 1$  °C with  $55 \pm 5\%$  humidity. The surgeries and experiments were performed in the light cycle. The animals were divided into three groups, i.e., sham, PLMC, and composite scaffolds, with each group containing three animals. All the animals were anesthetized on day 15 by injecting a cocktail of 80 mg/kg ketamine and 15 mg/kg xylazine intraperitoneally. The coat around the mid-dorsal area of anesthetized animals was shaven and sterilized with betadine, and a horizontal incision of approximately 1.5 cm was made in the skin with a sterile surgical blade to create a subcutaneous pocket. UV sterilized scaffolds were implanted inside the subcutaneous pocket, and the incision was closed with 4.0 sutures. No implantation was done in sham control rats. At the end of 15 days, the animals were sacrificed, and the skin tissue around the implant site was excised and preserved in formalin solution (10% in PBS). Vital organs, such as the kidney and liver, were also taken out for evaluation and preserved in the formalin solution. The fixed tissue was then embedded in paraffin, and tissue sections of 5  $\mu$ m were prepared by microtome. The obtained sections were stained with hematoxylin and Eosin (H&E) and imaged under a light microscope (IX-53, Olympus).

To assess any inflammatory response, hematological parameters were also checked. On day 7 and day 15, 1 ml of blood was collected from each animal. The blood was collected in heparin-coated tubes for the estimation of Total Leukocyte Count (TLC), Erythrocyte Sedimentation Rate (ESR), Serum glutamic pyruvic transaminase (SGPT) and Serum Glutamic-Oxaloacetic Transaminase (SGOT).

## 2.9 Statistical analysis

The results are presented as mean  $\pm$  standard error for each group. GraphPad Prism 5.04 was used for the statistical analysis (GraphPad Software, San Diego, CA, USA). One-way ANOVA was used for the statistical analysis, which was then followed by Dunnett and Tukey tests for significance. All analyses were carried out at a 95% confidence level and were significant at statistical probability (p-value)  $<0.05$ . Statistical significances were denoted as (\*), (\*\*) and (\*\*\*) for  $p < 0.05$ ,  $p < 0.01$  and  $p < 0.001$ , respectively.

## 3. Results and discussion

PLMC typically exhibits glass transition in the broad range of 20°C to 45°C, depending on its molecular weight, monomer (lactide(L): trimethylene carbonate(TMC)) ratio<sup>28</sup>, etc. The ratio of L:TMC was 70:30 in the copolymer used in this study. PLMC-Fe<sub>3</sub>O<sub>4</sub> composites containing 2.5%, 5%, and 10% (by weight) Fe<sub>3</sub>O<sub>4</sub> nanoparticles (diameter in the range of 50-100 nm) were prepared by solvent casting. 10% composites were difficult to print because of frequent clogging of the nozzles during printing owing to high melt viscosity. 2.5% composite structures exhibited minimal shape recoveries under magnetic field, as the particle content was low. Hence, 5% content was determined to be optimal as it was easily processable by printing and exhibited good shape recoveries. Only the 5% composite was used for further studies.

As seen from figure 2a, DSC thermograms reveal the  $T_g$  of PLMC to be  $\approx 33^\circ\text{C}$ , whereas that of the PLMC- $\text{Fe}_3\text{O}_4(5\%)$  composite is marginally lower (by  $3^\circ$ ) at  $30^\circ\text{C}$ . This change is attributed to the plasticizing effect of the nanoparticles, which reduces the thermal energy required for the segmental motions of the polymer chains<sup>29</sup>. Both the PLMC and nanocomposites also exhibit cold crystallization at  $\approx 112^\circ\text{C}$  and  $\approx 95^\circ\text{C}$ , respectively, due to the formation of crystals from the quenched-in amorphous structure above  $T_g$ <sup>30</sup>. Melting of PLMC occurs at  $154^\circ\text{C}$ , whereas the composite at  $158^\circ\text{C}$ , which is due to increased melt viscosity of the composite in the presence of nanoparticles. While some studies report PLMC to be amorphous<sup>28</sup>, other studies indicate its semi-crystalline nature<sup>31</sup>. Hence, the crystallinity depends on the molecular weight, polymerization kinetics, etc. The PLMC used in this study did exhibit sharp melting peaks in the DSC analysis.

Figure 2b reveals the  $\tan \delta$  values of PLMC and its composite, as recorded from temperature sweeps performed by DMA (dynamic mechanical analysis).  $T_g$  calculated from the peak of  $\tan \delta$  of PLMC is  $53^\circ\text{C}$ , whereas it is  $51^\circ\text{C}$  for the composite. It is to be noted that DSC captures the thermal transitions in a polymer alone, without accounting for mechanical forces which might influence the  $T_g$  values. In contrast, DMA is a more sensitive technique that captures the mechanical vibrations inside the polymer chains along with the thermal transitions, thereby resulting in different and higher  $T_g$  values than from DSC<sup>32</sup>. Also, the polymer specimen remains stretched in DMA, whereas DSC measures the  $T_g$  of unstretched samples<sup>33</sup>.

The TGA (thermogravimetric analysis) results indicate that thermal degradation of PLMC starts at  $\approx 240^\circ\text{C}$  while the composite starts to degrade at  $\approx 285^\circ\text{C}$ , as observed in figure 2c. These data aid in determining the optimal printing temperatures and times to minimize thermal degradation of the materials during melt extrusion-based 3D printing. TGA also confirmed the nanofiller content in the polymer matrix to be  $\approx 5\%$ . As observed in figure 2d, the DTG

(derivative thermogravimetric analysis) curves show the temperature of maximum decomposition rate for PLMC to be 300°C and composite to be 310°C.

Figure S1 confirms the structure of iron oxide nanoparticles from XRD and morphology from SEM. FTIR results in Figure S2 show the absence of any new chemical bond formation following the incorporation of nanoparticles in the PLMC matrix. This lack of interaction is due to the absence of functionalization in the particles, which only allows physical interaction with the polymer matrix. The peaks at 1085, 1187, and 1746  $\text{cm}^{-1}$  correspond to C-O stretching, C-C stretching, and  $\text{-C=O}$  vibration, respectively, in both neat PLMC and the composite samples corroborating the data from other studies on PLMC reported in the literature<sup>16</sup>. SEM images of the 3D printed composite structures confirm the excellent printability by extrusion printing technique.

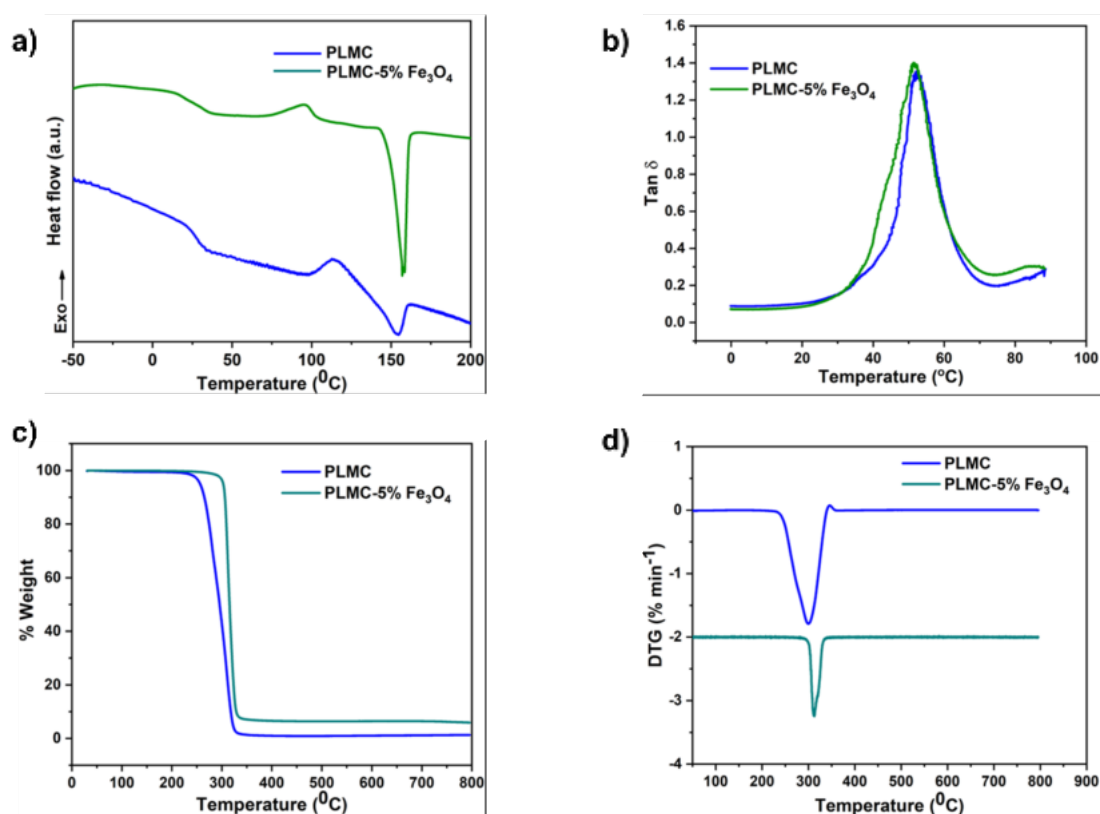




Figure 2: Thermal and dynamic thermo-mechanical characterizations of PLMC and its composite. a) DSC thermograms, b)  $\tan \delta$  (damping factor) as a function of temperature, c) TGA curves, and d) DTG curves versus temperature.

Figure 3 compiles the shape memory characteristics of neat PLMC and its magnetic nanocomposite. As calculated from the shape memory testing routines, PLMC exhibited excellent shape fixing of  $\approx 95\%$  and shape recovery of  $\approx 99\%$ . Similarly, the PLMC-Fe<sub>3</sub>O<sub>4</sub> composite exhibited  $\approx 97\%$  shape fixing and  $\approx 99\%$  shape recovery. The slightly enhanced shape fixing in the composite could be due to increased resistance in polymer chain motions offered by the stiff nanofillers below  $T_g$ . It is to be noted that shape recovery of PLMC starts at  $44^\circ\text{C}$  and composite at  $41^\circ\text{C}$ , as indicated by shape recovery onset temperature ( $T_s$ ) in figure 3 (b and d).  $T_s$  can differ from  $T_g$  and indicates the temperature at which macroscopic shape recovery occurs. It can also be observed from figure S3 that the storage modulus exhibits a sharp drop with an increase in temperature. Cyclic thermomechanical testing was also performed for both the materials for up to three cycles, as shown in figure S3. It is observed that PLMC sustained good fixing and recovery ratios, except for the first cycle<sup>34</sup>. The composite displayed excellent shape fixing and recovery ratios for the first cycle with a reduction in the properties in the subsequent cycles. It is known that the cyclic shape memory performance is highly dependent on testing parameters such as deformation rate, fixing temperature, recovery time, etc<sup>35</sup>. Hence, these results may vary with different testing conditions.

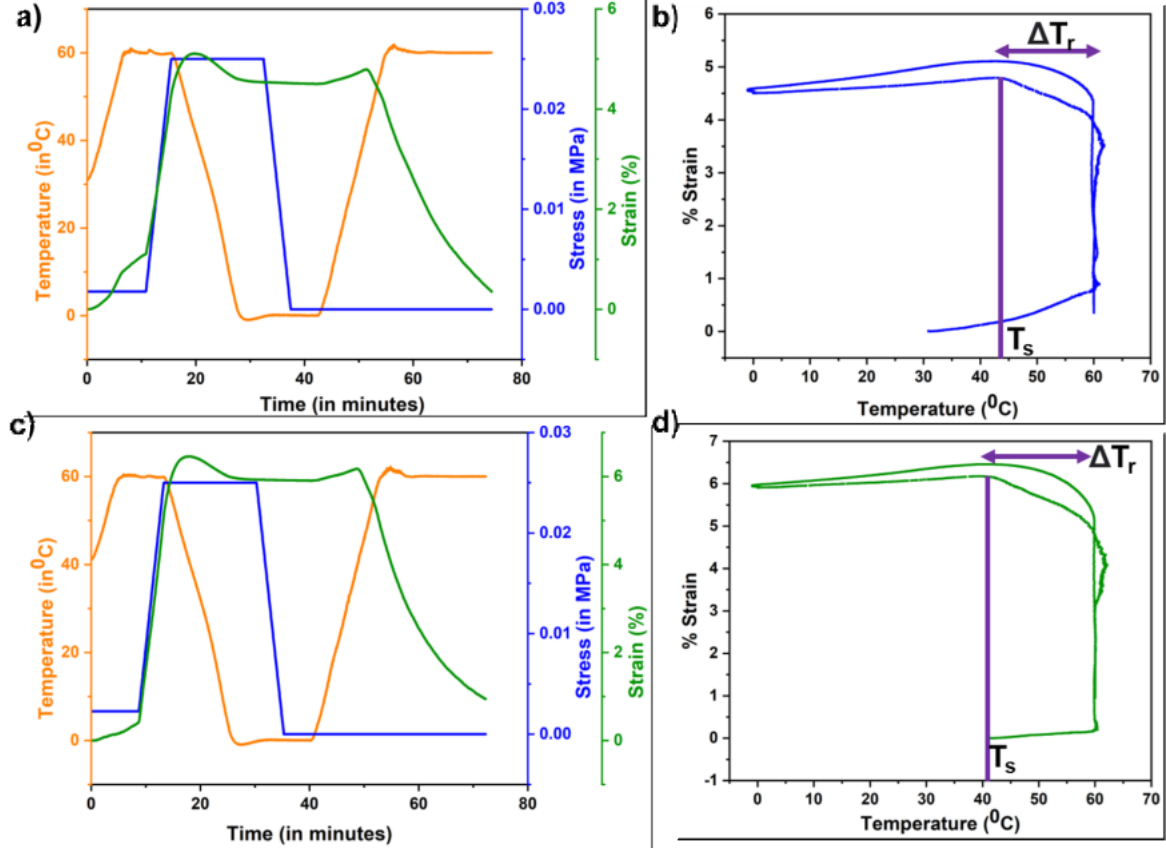


Figure 3: Shape memory characterization of PLMC and its composite. a) Thermomechanical shape memory testing of PLMC, b) strain profile of PLMC with temperature, c) Thermomechanical shape memory testing of PLMC composite, d) strain profile of PLMC composite with temperature.

Next, PLMC-5%  $\text{Fe}_3\text{O}_4$  composites were 3D printed into planar (2D) shapes and fixed into temporary shapes below  $T_g$ . Upon placing them in an alternating magnetic field, they recovered back to their original shapes by inductive heating, as shown in figure S4. It is due to the fact that  $\text{Fe}_3\text{O}_4$  nanoparticles act as localized heating sources inside the composite, and once the temperature reaches sufficiently above  $T_g$ , the composite macroscopically changes its shape to recover to its initial confirmation. The extent of recovery was around 95% for all the shapes, and recovery time was 45 to 60 s.

3D constructs of these composites were also printed wherein specific infill patterns (rectilinear) and densities (30%) were used to lay down material, as these infill parameters are most common in literature. The printed 3D constructs were fixed at 0°C and then were able to recover to their original shapes on magnetic actuation. In contrast to 2D shapes, 3D constructs were able to recover much faster (under 15 s) and better (>99%), as shown in figure 4 and supplementary videos V4, V5 and V6. This is because of a higher amount of material which corresponds to a higher number of heating elements and a higher specific absorption rate (SAR)<sup>36</sup>. SAR is defined as the rate of thermal energy dissipated by a material under an alternating magnetic field<sup>37</sup>.

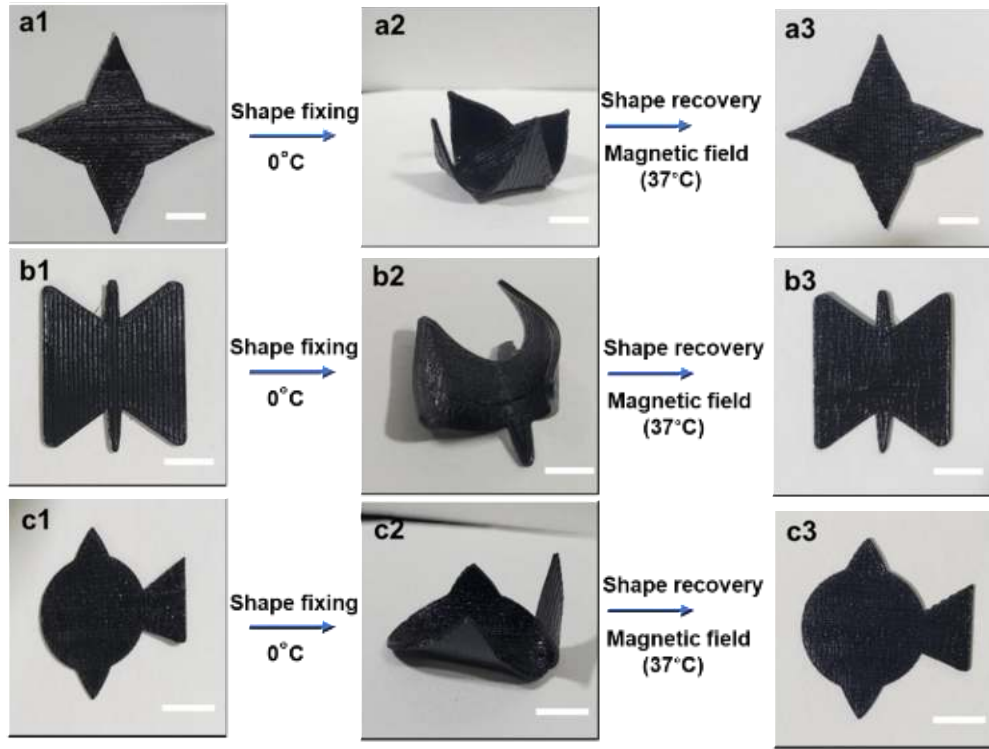


Figure 4: Shape recovery of 3D printed PLMC-5% Fe<sub>3</sub>O<sub>4</sub> (3D structures) under alternating magnetic field; a1) As printed petal shape, a2) Deformed and fixed (<T<sub>g</sub>) petal, a3) Recovered (>T<sub>g</sub>) petal, b1) As printed butterfly shape, b2) Deformed and fixed (<T<sub>g</sub>) butterfly, b3) Recovered (>T<sub>g</sub>) butterfly, c1) As-printed fish shape, c2) Deformed and fixed (<T<sub>g</sub>) fish, c3) Recovered (<T<sub>g</sub>) fish (Scale bar is 10 mm)

The particle size, concentration, and distribution of nanofillers in SMP directly impact the recovery performance and time<sup>38</sup>. Different studies report a minimum of 10 to 15 wt% of Fe<sub>3</sub>O<sub>4</sub> nanoparticles in the SMP matrix to trigger sufficient inductive heating and shape recovery<sup>39</sup>. However, in this study, only 5 wt% concentration of nanoparticles was sufficient to realize shape recovery in the SMP by the magnetic field. This is highly advantageous because of better dispersions, reduced agglomeration, and ease of processability. Moreover, a higher loading of nanoparticles may adversely affect cell viability.<sup>40</sup>

For *in vivo* applications, direct heating is not feasible owing to the poor thermal conductivity of polymers which then warrants the surrounding regions to be heated high enough to trigger shape recovery. Moreover, the tissues deep inside are not accessible to trigger shape recovery through contact heating. Magnetic composites offer a potential benefit allowing for a contactless recovery through inductive heating, which is very localized and doesn't require heating of the neighboring tissues. Figure 5a shows 3D printed composite scaffolds (printed using a 30% rectilinear infill pattern), which in their original disc confirmation, are not deployable. They could be easily deformed and fixed into flattened discs, which could now be delivered inside a tube. The scaffolds showed excellent shape recovery (>99%) under 15 s inside a magnetic field, as shown in video V7. The corresponding thermal images in figure S5 show the maximum temperature at the core of the scaffold is 40°C after complete recovery. In another case, the composites printed and fixed into tubular shapes could recover when constricted inside a glass tube within 10 s, as shown in figure 5b and video V8. This proof-of-concept demonstrates the potential of exploiting such materials as self-fitting scaffolds for various tissues. Apart from offering a benign actuation strategy, magnetic composites can also be remotely guided by permanent magnets to the site of deployment, as shown in video V8.



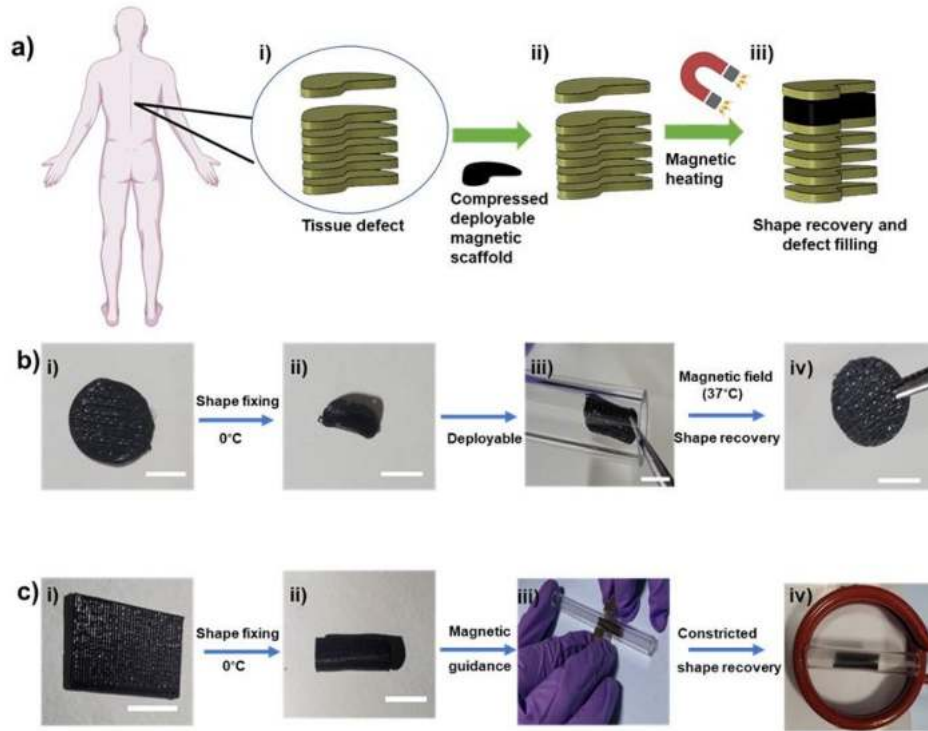


Figure 5: a) Schematic highlighting deployable tissue scaffolds. i) Tissue defect inside the human body, ii) 3D printed composite scaffold compressed and deployed in a minimally-invasive manner, iii) Inductive heating to trigger shape recovery of the magnetic scaffold and confirm to defect shape; b) Shape recovery of 3D printed PLMC-5% Fe<sub>3</sub>O<sub>4</sub> composites as deployable tissue scaffolds under alternating magnetic field. i) As-printed disc-shaped scaffold, ii) Scaffold is not able to pass through a tube in original conformation, iii) Deformed and fixed scaffold ( $<T_g$ ), iv) Fixed scaffold able to be deployed through tube ( $>T_g$ ), v) Recovered scaffold (Scale bar is 5 mm); c) Restrictive shape recovery of pre-programmed shape to original shape; c) As-printed PLMC-5% Fe<sub>3</sub>O<sub>4</sub> composite, ii) Deformed and fixed shape, iii) Magnetically guided and recovery of pre-programmed structure into original shape under alternating magnetic field. (Scale bar is 10 mm)

Next, neat PLMC and PLMC magnetic composites were used to print specific parts inside a single structure, as shown in figure 6. The structures were deformed and fixed into pre-programmed shapes below the  $T_g$ . The portions printed with the composite only recovered inside an alternating magnetic field, as neat PLMC is not magnetically responsive (as shown in videos V9-V12 for a variety of structures). The partially recovered structures are stable unless a direct heating stimulus is provided when PLMC parts also begin to recover yielding completely recovered structures. This offers sequential and selective stimulation of parts in a structure. Such concepts could find use in soft robotics<sup>41-42</sup>, grippers<sup>43-44</sup>, etc., wherein distinct regions of a macro-structure need to be actuated at one time.

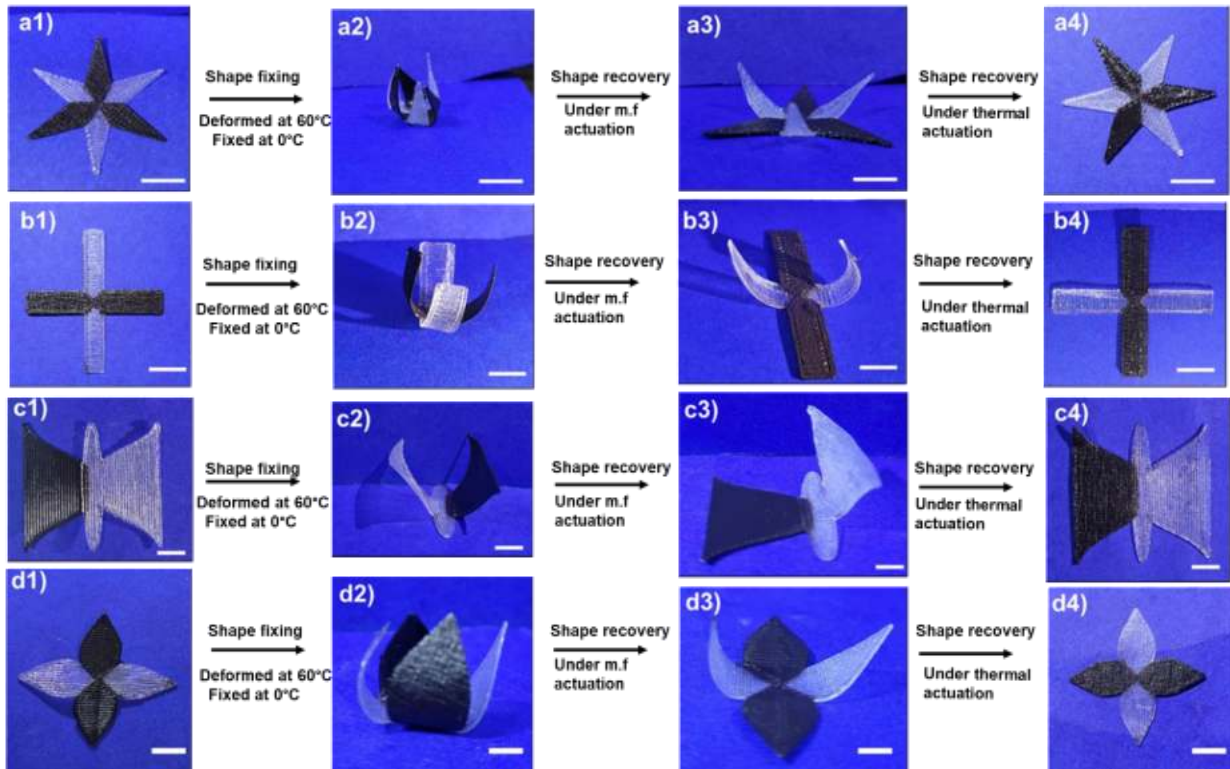


Figure 6: Shape recovery of 3D printed PLMC and PLMC-5%  $\text{Fe}_3\text{O}_4$  composite dual structures sequentially and selectively actuated under alternating magnetic field and then heat; a1) Dual-printed star, a2) Deformed star, a3) Partially recovered star by indirect heating, a4) Fully recovered star by direct heating, b1) Dual-printed cross, b2) Deformed cross, b3) Partially recovered cross by indirect heating, b4) Fully recovered cross by direct heating, c1)

Dual-printed butterfly, c2) Deformed butterfly, c3) Partially recovered butterfly by indirect heating, c4) Fully recovered butterfly by direct heating, d1) Dual-printed petal, d2) Deformed petal, d3) Partially recovered petal by indirect heating, d4) Fully recovered petal by direct heating (Scale bar is 10 mm)

Next, the *in vitro* biocompatibility of the materials was assessed using NIH 3T3 cells. The results of cytocompatibility analysis are compiled in figure 7. Live/dead staining (figure 7a) demonstrated that both PLMC and composite did not show any toxicity to the cultured cells. Most of the cells were viable with very minimal cell death. Also, the cells adhered and proliferated in number over time on both the materials, as seen from the Alamar blue assay (figure 7b), indicating excellent biocompatibility. Further, cytoskeletal staining on different days (figure 7c) demonstrates that cells could adhere and spread on the surface of the materials.

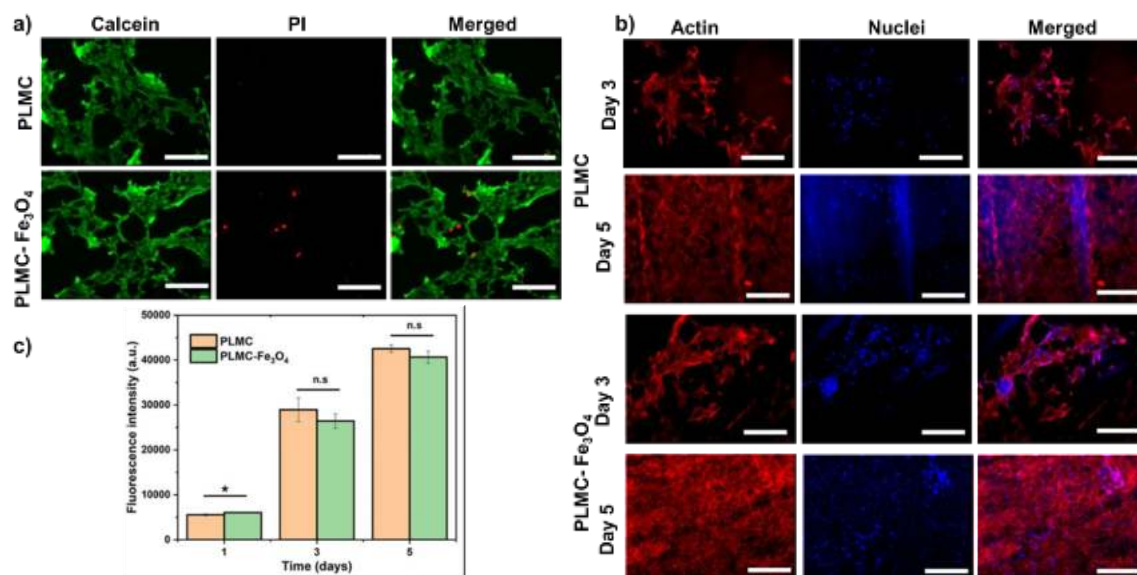


Figure 7: *In vitro* biological characterization of PLMC and its composite. a) Live-dead assay, b) Cytoskeletal staining, and c) Alamar blue assay. \* denotes  $p < 0.05$ , n.s is non-significant.

(Scale bar is 100  $\mu\text{m}$ )

Since this nanocomposite has great potential to be extended for biomedical applications, *in vivo* biocompatibility was also assessed in Wistar rats. The results of *in vivo* biocompatibility are compiled in figure 8. Histological observations on different days post-implantation (Days 7 and 14) demonstrated that both PLMC and the nanocomposite did not elicit any major inflammatory tissue response at the site of implantation. The surrounding skin displayed healthy physiology with loosely packed extracellular matrix (ECM), skin appendages, and the absence of infiltrating inflammatory cells. Further, to confirm the inflammatory response from scaffold remnants and/or degraded products, histological observations of two vital organs, the liver and kidney, were also observed. As seen in Figure 7, healthy physiology of both organs was observed with no signs of inflammation. Normal lobular morphology of the liver and the characteristic kidney morphology with intact glomerulus and glomerular-capsular space in Sham, PLMC, and composite groups. Further, normal blood parameters in all groups confirmed the absence of any cytotoxicity induced by the implanted polymers (figure S6).



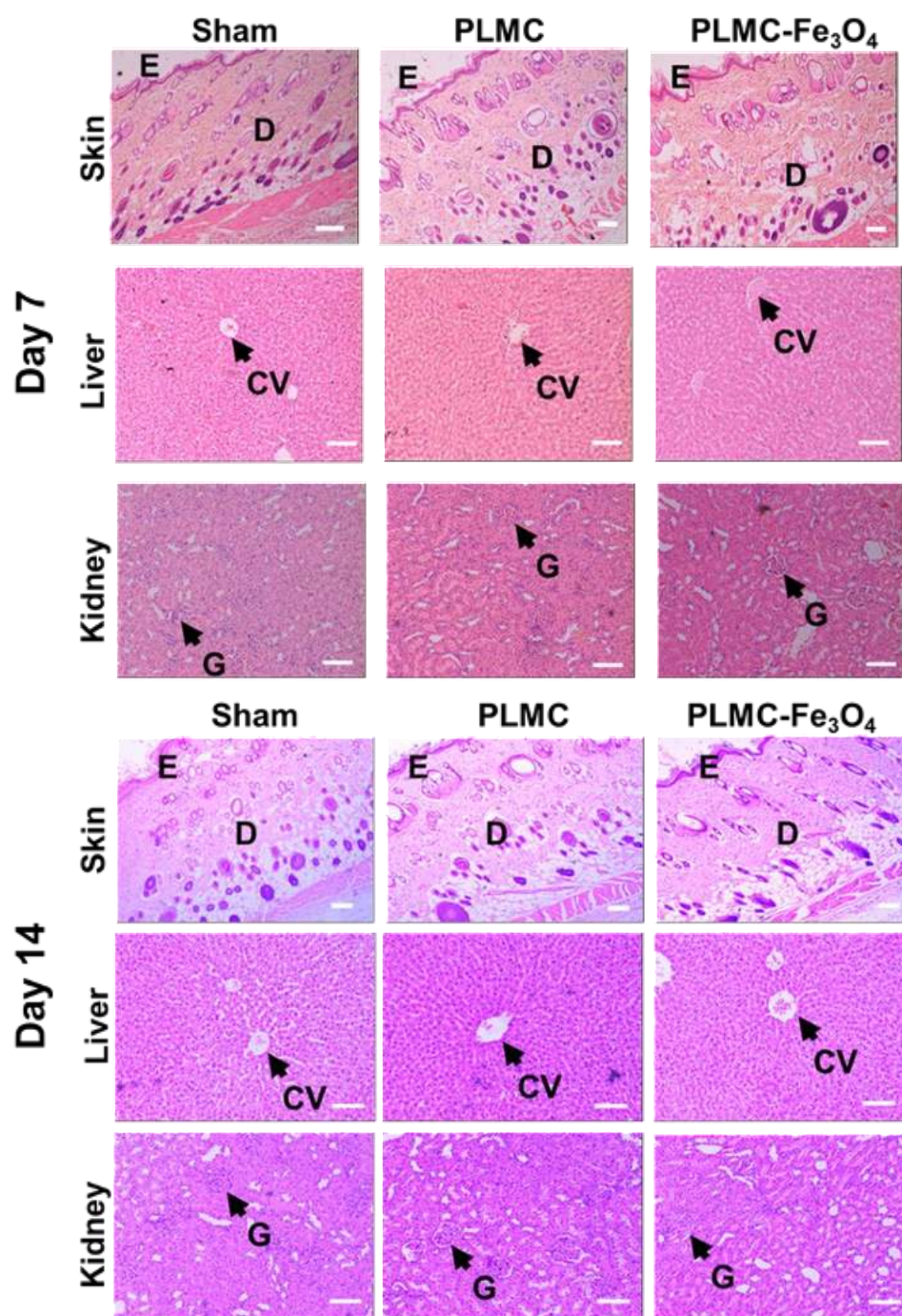


Figure 8: *In vivo* biological characterization of PLMC and composites. Histological staining of skin, liver, and kidney sections in Sham, PLMC, and nanocomposite groups on day 7 and day 14 (scale bar is 100  $\mu$ m for all images except for skin tissues, where the scale bar is 200  $\mu$ m).

The distinct advantages of our material system are excellent shape recoveries (>99%), and extremely fast (under 15 s for 3D structures) at physiological temperatures ( $\approx 37^{\circ}\text{C}$ ), which are ideal for biomedical applications. Extrusion-based printing was used, which is advantageous over other strategies like direct ink writing, which involve toxic solvents and post-processing steps. Also, the concentration of  $\text{Fe}_3\text{O}_4$  nanofillers used is very low (i.e., 5% w/w) compared to other studies, which report at least 15% (w/w). Lower filler concentrations are always advantageous because of easy processability and lower risks of associated nanotoxicities<sup>45</sup>. The magnetic composites were printed into 3D porous scaffolds that could be potentially deployed to the site of tissue defects and triggered through inductive heating to conform to the defect size. *In vitro* and *in vivo* biocompatibility of PLMC and its composites were assessed to highlight the importance of the material systems as deployable tissue scaffolds. Additionally, PLMC and PLMC-  $\text{Fe}_3\text{O}_4$  composites were printed selectively in different regions of the same structure to have sequential and selective stimulation under heating and magnetic field actuation, respectively.

## Conclusion

In this study, novel PLMC- 5%  $\text{Fe}_3\text{O}_4$  composites were 3D printed via extrusion-based printing. The printed composites exhibited excellent shape fixity ratios ( $\approx 95\%$ ) and shape recovery ratios ( $\approx 99\%$ ) for both 2D and 3D shapes. The key advantages were short recovery times (under 15 s) at physiologically relevant recovery temperatures ( $\approx 40^{\circ}\text{C}$ ). The composites were also printed into porous tissue scaffolds. The scaffolds were compressed into shapes that can be deployable in a minimally invasive manner, magnetically guided, and were recovered ( $\approx 99\%$ ) by inductive heating to original shapes. The composites showed favorable *in vitro* and *in vivo* biocompatibility. These features make it highly conducive for being employed as self-fitting scaffolds and other biomedical applications. Neat PLMC and PLMC composites were used to print distinct regions in a single structure, which then exhibited selective and sequential

recovery through direct and inductive heating. Taken together, PLMC-based magnetic nanocomposites pave the way for a multitude of applications spanning robotics, advanced manufacturing, biomedical areas, etc. that demand excellent and fast shape recoveries with complex geometries.

## Acknowledgements

The authors thank the Department of Science and Technology (DST) (DST/NM/NB/2018/119(G)) and the Science and Engineering Research Board (SERB) (IPA/2020/000025) for the financial support. We acknowledge Dr. Suhela Tyeb for her help in animal studies. We thank Central Animal Facility (CAF) for extending the facilities for animal studies. S.C. acknowledges support from the Prime Minister's Research Fellowship. A.J. acknowledges IoE fellowship from IISc.

## References:

1. Panda, B.; Paul, S. C.; Hui, L. J.; Tay, Y. W. D.; Tan, M. J., Additive manufacturing of geopolymer for sustainable built environment. *Journal of Cleaner Production* **2017**, *167*, 281-288.
2. Bhatt, P. M.; Malhan, R. K.; Shembekar, A. V.; Yoon, Y. J.; Gupta, S. K., Expanding capabilities of additive manufacturing through use of robotics technologies: A survey. *Additive Manufacturing* **2020**, *31*, 100933.
3. Ramola, M.; Yadav, V.; Jain, R., On the adoption of additive manufacturing in healthcare: a literature review. *Journal of Manufacturing Technology Management* **2018**.
4. Choi, J.; Kwon, O.-C.; Jo, W.; Lee, H. J.; Moon, M.-W., 4D printing technology: a review. *3D Printing and Additive Manufacturing* **2015**, *2* (4), 159-167.
5. Scalet, G. In *Two-way and multiple-way shape memory polymers for soft robotics: An overview*, Actuators, Multidisciplinary Digital Publishing Institute: 2020; p 10.
6. Ze, Q.; Kuang, X.; Wu, S.; Wong, J.; Montgomery, S. M.; Zhang, R.; Kovitz, J. M.; Yang, F.; Qi, H. J.; Zhao, R., Magnetic shape memory polymers with integrated multifunctional shape manipulation. *Advanced Materials* **2020**, *32* (4), 1906657.
7. Santo, L.; Quadrini, F.; Accettura, A.; Villadei, W., Shape memory composites for self-deployable structures in aerospace applications. *Procedia Engineering* **2014**, *88*, 42-47.
8. Delaey, J.; Dubruel, P.; Van Vlierberghe, S., Shape-memory polymers for biomedical applications. *Advanced Functional Materials* **2020**, *30* (44), 1909047.

9. Sun, L.; Huang, W.; Wang, C.; Zhao, Y.; Ding, Z.; Purnawali, H., Optimization of the shape memory effect in shape memory polymers. *Journal of Polymer Science Part A: Polymer Chemistry* **2011**, *49* (16), 3574-3581.
10. Yang, X.; Wang, L.; Wang, W.; Chen, H.; Yang, G.; Zhou, S., Triple shape memory effect of star-shaped polyurethane. *ACS Applied Materials & Interfaces* **2014**, *6* (9), 6545-6554.
11. Wu, Y.; Hu, J.; Zhang, C.; Han, J.; Wang, Y.; Kumar, B., A facile approach to fabricate a UV/heat dual-responsive triple shape memory polymer. *Journal of Materials Chemistry A* **2015**, *3* (1), 97-100.
12. Yakacki, C. M.; Shandas, R.; Lanning, C.; Rech, B.; Eckstein, A.; Gall, K., Unconstrained recovery characterization of shape-memory polymer networks for cardiovascular applications. *Biomaterials* **2007**, *28* (14), 2255-2263.
13. Huang, W. M.; Song, C. L.; Fu, Y. Q.; Wang, C. C.; Zhao, Y.; Purnawali, H.; Lu, H. B.; Tang, C.; Ding, Z.; Zhang, J. L., Shaping tissue with shape memory materials. *Advanced Drug Delivery Reviews* **2013**, *65* (4), 515-535.
14. Small Iv, W.; Wilson, T. S.; Benett, W. J.; Loge, J. M.; Maitland, D. J., Laser-activated shape memory polymer intravascular thrombectomy device. *Optics Express* **2005**, *13* (20), 8204-8213.
15. Hu, J.-J.; Lei, Q.; Zhang, X.-Z., Recent advances in photonanomedicines for enhanced cancer photodynamic therapy. *Progress in Materials Science* **2020**, *114*, 100685.
16. Wan, X.; Wei, H.; Zhang, F.; Liu, Y.; Leng, J., 3D printing of shape memory poly (d, l-lactide-co-trimethylene carbonate) by direct ink writing for shape-changing structures. *Journal of Applied Polymer Science* **2019**, *136* (44), 48177.
17. Dai, S.; Yue, S.; Ning, Z.; Jiang, N.; Gan, Z., Polydopamine Nanoparticle-Reinforced Near-Infrared Light-Triggered Shape Memory Polycaprolactone–Polydopamine Polyurethane for Biomedical Implant Applications. *ACS Applied Materials & Interfaces* **2022**, *14* (12), 14668-14676.
18. Li, G.; Yan, Q.; Xia, H.; Zhao, Y., Therapeutic-Ultrasound-Triggered Shape Memory of a Melamine-Enhanced Poly(vinyl alcohol) Physical Hydrogel. *ACS Applied Materials & Interfaces* **2015**, *7* (22), 12067-12073.
19. Liu, W.; Wang, A.; Yang, R.; Wu, H.; Shao, S.; Chen, J.; Ma, Y.; Li, Z.; Wang, Y.; He, X., Water-triggered stiffening of shape memory polyurethanes composed of hard backbone dangling PEG soft segments. *Advanced Materials* **2022**, 2201914.
20. Yu, K.; Liu, Y.; Leng, J., Shape memory polymer/CNT composites and their microwave induced shape memory behaviors. *Rsc Advances* **2014**, *4* (6), 2961-2968.
21. Soto, G. D.; Meiorin, C.; Actis, D. G.; Mendoza Zélis, P.; Moscoso Londoño, O.; Muraca, D.; Mosiewicki, M. A.; Marcovich, N. E., Magnetic nanocomposites based on shape memory polyurethanes. *European Polymer Journal* **2018**, *109*, 8-15.
22. Gu, S.-Y.; Chang, K.; Jin, S.-P., A dual-induced self-expandable stent based on biodegradable shape memory polyurethane nanocomposites (PCLAU/Fe<sub>3</sub>O<sub>4</sub>) triggered around body temperature. *Journal of Applied Polymer Science* **2018**, *135* (3), 45686.
23. Mohr, R.; Kratz, K.; Weigel, T.; Lucka-Gabor, M.; Moneke, M.; Lendlein, A., Initiation of shape-memory effect by inductive heating of magnetic nanoparticles in thermoplastic polymers. *Proceedings of the National Academy of Sciences* **2006**, *103* (10), 3540-3545.

24. Wei, H.; Zhang, Q.; Yao, Y.; Liu, L.; Liu, Y.; Leng, J., Direct-write fabrication of 4D active shape-changing structures based on a shape memory polymer and its nanocomposite. *ACS applied materials & interfaces* **2017**, *9* (1), 876-883.
25. Zhao, W.; Zhang, F.; Leng, J.; Liu, Y., Personalized 4D printing of bioinspired tracheal scaffold concept based on magnetic stimulated shape memory composites. *Composites Science and Technology* **2019**, *184*, 107866.
26. Zhang, F.; Wang, L.; Zheng, Z.; Liu, Y.; Leng, J., Magnetic programming of 4D printed shape memory composite structures. Elsevier: 2019.
27. Wan, X.; He, Y.; Liu, Y.; Leng, J., 4D printing of multiple shape memory polymer and nanocomposites with biocompatible, programmable and selectively actuated properties. *Additive Manufacturing* **2022**, *53*, 102689.
28. Bao, M.; Lou, X.; Zhou, Q.; Dong, W.; Yuan, H.; Zhang, Y., Electrospun biomimetic fibrous scaffold from shape memory polymer of PDLLA-co-TMC for bone tissue engineering. *ACS applied materials & interfaces* **2014**, *6* (4), 2611-2621.
29. Zheng, X.; Zhou, S.; Xiao, Y.; Yu, X.; Li, X.; Wu, P., Shape memory effect of poly (d, l-lactide)/Fe<sub>3</sub>O<sub>4</sub> nanocomposites by inductive heating of magnetite particles. *Colloids and Surfaces B: Biointerfaces* **2009**, *71* (1), 67-72.
30. Righetti, M. C., Crystallization of polymers investigated by temperature-modulated DSC. *Materials* **2017**, *10* (4), 442.
31. Fuoco, T.; Mathisen, T. r.; Finne-Wistrand, A., Poly (l-lactide) and poly (l-lactide-co-trimethylene carbonate) melt-spun fibers: structure–processing–properties relationship. *Biomacromolecules* **2019**, *20* (3), 1346-1361.
32. Ferrillo, R. G.; Achorn, P. J., Comparison of thermal techniques for glass transition assignment. II. Commercial polymers. *Journal of Applied Polymer Science* **1997**, *64* (1), 191-195.
33. Sharifi, S.; van Kooten, T. G.; Kranenburg, H.-J. C.; Meij, B. P.; Behl, M.; Lendlein, A.; Grijpma, D. W., An annulus fibrosus closure device based on a biodegradable shape-memory polymer network. *Biomaterials* **2013**, *34* (33), 8105-8113.
34. Sauter, T.; Heuchel, M.; Kratz, K.; Lendlein, A., Quantifying the Shape-Memory Effect of Polymers by Cyclic Thermomechanical Tests. *Polymer Reviews* **2013**, *53* (1), 6-40.
35. Hu, J. L.; Ji, F. L.; Wong, Y. W., Dependency of the shape memory properties of a polyurethane upon thermomechanical cyclic conditions. *Polymer International* **2005**, *54* (3), 600-605.
36. Weigel, T.; Mohr, R.; Lendlein, A., Investigation of parameters to achieve temperatures required to initiate the shape-memory effect of magnetic nanocomposites by inductive heating. *Smart Materials and Structures* **2009**, *18* (2), 025011.
37. Evans, B. A.; Bausch, M. D.; Sienerth, K. D.; Davern, M. J., Non-monotonicity in the influence of nanoparticle concentration on SAR in magnetic nanoparticle hyperthermia. *Journal of Magnetism and Magnetic Materials* **2018**, *465*, 559-565.
38. Ma, M.; Wu, Y.; Zhou, J.; Sun, Y.; Zhang, Y.; Gu, N., Size dependence of specific power absorption of Fe<sub>3</sub>O<sub>4</sub> particles in AC magnetic field. *Journal of Magnetism and Magnetic Materials* **2004**, *268* (1), 33-39.
39. Salkhi Khasraghi, S.; Shojaei, A.; Janmaleki, M.; Sundararaj, U., Efficient inductively heated shape memory polyurethane acrylate network with silane modified



- nanodiamond@Fe<sub>3</sub>O<sub>4</sub> superparamagnetic nanohybrid. *European Polymer Journal* **2021**, *159*, 110735.
40. Ghasempour, S.; Shokrgozar, M. A.; Ghasempour, R.; Alipour, M., Investigating the cytotoxicity of iron oxide nanoparticles in in vivo and in vitro studies. *Experimental and Toxicologic Pathology* **2015**, *67* (10), 509-515.
  41. Han, M.-W.; Ahn, S.-H., Blooming Knit Flowers: Loop-Linked Soft Morphing Structures for Soft Robotics. *Advanced Materials* **2017**, *29* (13), 1606580.
  42. Jin, B.; Song, H.; Jiang, R.; Song, J.; Zhao, Q.; Xie, T., Programming a crystalline shape memory polymer network with thermo- and photo-reversible bonds toward a single-component soft robot. *Science Advances* **2018**, *4* (1), eaao3865.
  43. Diller, E.; Sitti, M., Three-Dimensional Programmable Assembly by Untethered Magnetic Robotic Micro-Grippers. *Advanced Functional Materials* **2014**, *24* (28), 4397-4404.
  44. Abdullah, A. M.; Li, X.; Braun, P. V.; Rogers, J. A.; Hsia, K. J., Self-Folded Gripper-Like Architectures from Stimuli-Responsive Bilayers. *Advanced Materials* **2018**, *30* (31), 1801669.
  45. Soenen, S. J. H.; Nuytten, N.; De Meyer, S. F.; De Smedt, S. C.; De Cuyper, M., High Intracellular Iron Oxide Nanoparticle Concentrations Affect Cellular Cytoskeleton and Focal Adhesion Kinase-Mediated Signaling. *Small* **2010**, *6* (7), 832-842.